

## Summer 2005 update of the CKM angle $\gamma$ extraction in $B^- \rightarrow D^{(*)}K^{(*)-}$ decays using a $D^0$ Dalitz plot analysis technique

S. Bettarini<sup>1</sup>, M. Carpinelli<sup>1</sup>, G. Cavoto<sup>2</sup>, M. Giorgi<sup>1</sup>, Y.P. Lau<sup>3</sup>,  
L.Li Gioi<sup>2</sup>, F. Martinez-Vidal<sup>1,4</sup>, N. Lopez-March<sup>4</sup>, N. Neri<sup>1</sup>,  
J. Olsen<sup>3</sup>, S. Pruvot<sup>5</sup>, M. Rama<sup>1</sup>, M.H. Schune<sup>5</sup>, A. Stocchi<sup>5</sup>

<sup>1</sup>*Università di Pisa & INFN Pisa, Italy*

<sup>2</sup>*Università di Roma "La Sapienza" & INFN Roma I, Italy*

<sup>3</sup>*Princeton University, Princeton, NJ, USA*

<sup>4</sup>*IFIC/CSIC Valencia, Spain*

<sup>5</sup>*Laboratoire de l'Accélérateur Linéaire, Orsay, France*

### Abstract

This note describes the updated measurement of the CKM angle  $\gamma$  from the study of  $B^- \rightarrow D^{(*)}K^{*-}$  using a Dalitz plot analysis technique of  $D^0 \rightarrow K_S\pi^+\pi^-$  decays. In this updated measurement we add the  $B^- \rightarrow DK^{*-}$  decay mode and we use the K-matrix method to parametrize the  $D^0$  decay amplitude and evaluate the corresponding Dalitz model systematic error. We report on the selection of the  $B^- \rightarrow DK^{*-}$  signal events, background characterization and on the  $CP$  likelihood fit and systematic error evaluation. For this analysis we have used the Run1-2-3-4 data sample, corresponding to an integrated luminosity of  $208 \text{ fb}^{-1}$ .

# Contents

<b>1</b>	<b>Selection of the <math>B^- \rightarrow D^0 K^{*-}</math> events</b>	<b>5</b>
1.1	Reconstruction release and data sample . . . . .	5
1.2	Selection criteria . . . . .	5
1.3	Background characterization . . . . .	10
1.4	Best candidate choice . . . . .	12
1.5	Data/Monte Carlo comparison . . . . .	12
<b>2</b>	<b>PDF for <math>B^- \rightarrow D^0 K^{*-}</math> decays</b>	<b>15</b>
<b>3</b>	<b><math>CP</math> fit</b>	<b>18</b>
3.1	Inputs . . . . .	20
3.1.1	Selection PDF shapes . . . . .	20
3.1.2	Efficiency and Background Dalitz shapes . . . . .	22
3.1.3	$D^0$ fractions . . . . .	23
3.1.4	Fraction of wrong sign signal ( $\kappa_{\text{sigWS}}$ ) . . . . .	23
3.2	Results from PDF shapes fit . . . . .	23
3.3	Results from $CP$ fit . . . . .	27
3.4	Nominal Toy Monte Carlo . . . . .	27
<b>4</b>	<b>Experimental systematic uncertainties</b>	<b>37</b>
4.1	$m_{\text{ES}}$ and Fisher shapes . . . . .	37
4.2	Background composition . . . . .	37
4.3	Dalitz efficiency . . . . .	38
4.4	Dalitz shape for combinatorial background . . . . .	38
4.5	Limited mass resolution . . . . .	38
4.6	Statistical errors on Dalitz amplitudes and phases . . . . .	39
4.7	Wrong sign signal fraction . . . . .	39
<b>5</b>	<b>Dalitz model systematic uncertainty</b>	<b>40</b>
<b>6</b>	<b>Frequentist interpretation of the results</b>	<b>50</b>
<b>A</b>	<b>Model dependent parametrization of the <math>B^- \rightarrow D^0 K^{*-}</math> amplitude</b>	<b>56</b>
<b>B</b>	<b>Considerations on the efficiency variation over the <math>B^- \rightarrow D^0 K_S^0 \pi^-</math> Dalitz plot</b>	<b>58</b>

## Summary

- 31 May 2005: This first version of the note focuses on the selection of the  $B^- \rightarrow D^0 K^{*-}$  events and on the  $CP$  likelihood fit. In it we described the PDF for signal events including the non-resonant  $B^- \rightarrow D^0 K_s^0 \pi^-$  contribution to the decay and the evaluation of the related systematic error. The systematic error due to the dalitz model parameterization and to the fit method have still to be evaluated.
- 7 June 2005: In this second version we take into account all the AWG readers (Richard Kass and Owen Long) comments. We have changed the PDF for the  $CP$  fit and we use a 2D PDF with  $m_{ES}$  and Fisher variables instead of a 3D PDF which included also  $\Delta E$ . We fit for the  $r_s^2$  parameter therefore we canceled the systematic error due to the non-resonant contribution. The main experimental systematic errors have been evaluated, the Dalitz model error is still work in progress.
- 29 June 2005: Include the evaluation of the Dalitz model systematic error using the alternative K-Matrix and CLEO model parameterizations.
- 05 June 2005: Frequentist  $\gamma$  extraction using a combined PDF with  $B^- \rightarrow D^{(*)0} K^-$  and  $B^- \rightarrow D^0 K^{*-}$  measurements. Include RC comments and suggestions.

## Introduction

The angle  $\gamma$  of the unitarity triangle [1] is related to the complex phase of the CKM element  $V_{ub}$  through the relation  $V_{ub} = |V_{ub}|e^{-i\gamma}$ . Various methods have been proposed to extract  $\gamma$  using  $B^\pm \rightarrow DK^\pm$  decays, all exploiting the interference between the color allowed  $B^- \rightarrow D^0 K^-$  ( $\propto V_{cb}$ ) and the color suppressed  $B^- \rightarrow \bar{D}^0 K^-$  ( $\propto V_{ub}$ ) transitions, when the  $D^0$  and  $\bar{D}^0$  are reconstructed in a common final state. The extraction of  $\gamma$  with these decays is theoretically clean because the main contributions to the amplitudes come from tree-level diagrams; for the same reason, effects from new physics are negligible in most of the models beyond the SM.

Among the  $D$  decay modes studied so far,  $D^0 \rightarrow K_s^0 \pi^- \pi^+$  is the one with the highest sensitivity to  $\gamma$  because of the best overall combination of branching ratio magnitude,  $D^0/\bar{D}^0$  interference and background level. BaBar presented a preliminary measurement of  $\gamma$  based on Run1-4 data with  $B^- \rightarrow D^{(*)0} K^-$ , where  $D^{*0} \rightarrow \pi^0/\gamma$  and  $D^0 \rightarrow K_s^0 \pi^- \pi^+$ , at ICHEP 2004[2]. The measurement was submitted to Phys. Rev. Letters in April 2005 [3].

The main improvements for Summer 2005 are the addition of the  $B^- \rightarrow D^0 K^{*-}$  decay mode and the investigation of the  $K$ -matrix formalism to describe the  $D^0 \rightarrow K_s^0 \pi^- \pi^+$  Dalitz plot. The measurement of  $B^- \rightarrow D^0 K^{*-}$  will be combined to the already measured  $B^- \rightarrow D^{(*)0} K^-$  to quote an update of the  $\gamma$  measurement.

This note describes the selection, background characterization and  $CP$  fit of  $B^- \rightarrow D^0 K^{*-}$  with  $K^{*-} \rightarrow K_s^0 \pi^-$ . The analysis structure is very similar to the  $B^- \rightarrow D^{(*)0} K^-$  analysis described in [4], with the addition of the treatment of the  $B^- \rightarrow DK_s^0 \pi^-$  non-resonant contribution. The  $K^{*-} \rightarrow K^- \pi^0$  was also investigated, but due to the lower signal rate and higher background level we decided to postpone its measurement to after the Summer. The study of the  $D$  Dalitz plot with the  $K$ -matrix model is described in a separate document, BAD1237 [5].

# 1 Selection of the $B^- \rightarrow D^0 K^{*-}$ events

In this section we describe the selection of the  $B^- \rightarrow D^0 K^{*-}$  events with  $K^{*-} \rightarrow K_S \pi^-$ ,  $D^0 \rightarrow K_S \pi^+ \pi^-$ . We discuss the optimization of the cuts and the background parameterization. This analysis is very similar to the  $B^- \rightarrow D^{(*)0} K^-$  analysis, documented in [4]. We have used the same Fisher discriminant  $\mathcal{F}$  as in the  $B^- \rightarrow D^{(*)0} K^-$  analysis and we have applied the same cut on  $|\cos \theta_T| < 0.8$

## 1.1 Reconstruction release and data sample

We have used for the rootuple production the physics release analysis-23, aka 14.5.5. We have analyzed events from the skimmed `BchToD0KstarAll` collections, whose selection criteria are described in [6]. The amount of on-resonance data reduces to 2.8% with processing time of 2.2 ms/event. The efficiency on signal Monte Carlo events after the wide skim cuts is about 24% including detector and reconstruction efficiencies. We have used all the Run1-Run4 available data sample for this analysis for On-peak and Off-peak data and a large Monte Carlo sample for background studies, as reported in Table 1. We have used a large Monte Carlo sample of signal events  $\text{Sig}_{ps}$ , to evaluate the efficiency in the Dalitz plane. It has  $D^0$  phase space distributed events and also the  $B$  decays according to a phase space distribution.<sup>1</sup> Two different samples  $\text{Sig}_{hel1}$ ,  $\text{Sig}_{hel2}$  with angular distribution according to the `SVS` model for the decay  $B^- \rightarrow D^0 K^{*-}$ , has been used to optimized the selection cuts. Both  $\text{Sig}_{hel1}$  and  $\text{Sig}_{hel2}$  let the  $K^{*-}$  to decay into the generic mode according to an identical decay tree but they were available at different time.

Sample	Events	Luminosity ( $\text{fb}^{-1}$ )
$B^0 \bar{B}^0$	542.5M	986
$B^+ B^-$	542.5M	986
$c\bar{c}$	393.0M	301
$u\bar{u}, d\bar{d}, s\bar{s}$	710.0M	339
$\text{Sig}_{hel1}$	4600	1458
$\text{Sig}_{hel2}$	6900	2169
$\text{Sig}_{ps}$	115K	76248
Data (On-peak)		208.4
Data (Off-peak)		21.6

Table 1: *Number of generated Monte Carlo events for signals and backgrounds and corresponding integrated luminosities. The integrated luminosity for data is also given.*

The various assumptions for the branching fractions and cross sections used to get the values of Table 1 are summarized in Table 2. These values have been used to normalize the signal and the different background components.

## 1.2 Selection criteria

We optimize the selection criteria in order to reconstruct an event sample which minimizes the error on  $\gamma$ . It has been shown in BAD899 that the sensitivity on  $\gamma$ , once the signal yield is fixed, depends on the level of background and at first order it doesn't depend on the composition of the

---

<sup>1</sup>It has been checked that the phase space distribution of the  $B$  does not affect the evaluation of the efficiency map in the  $D^0$  Dalitz plane.

Quantity	Value
$\sigma(b\bar{b})$	1.10 nb
$\sigma(c\bar{c})$	1.30 nb
$\sigma(u\bar{u}, d\bar{d}, s\bar{s})$	2.09 nb
$Br(B^- \rightarrow D^0 K^{*-})$	$(6.1 \pm 2.3) \cdot 10^{-4}$ [7]
$Br(D^0 \rightarrow \bar{K}^0 \pi^- \pi^+)$	$0.0597 \pm 0.0035$ [7]
$Br(\bar{K}^0 \rightarrow K_S^0)$	1/2
$Br(K_S^0 \rightarrow \pi^+ \pi^-)$	$0.6895 \pm 0.0014$ [7]
$Br(B^- \rightarrow D^0 \pi^-)$	$(4.98 \pm 0.29) \cdot 10^{-3}$ [7]

Table 2: Branching fractions and cross sections used to get the values of Table 1. These values have been used to normalize the signal and the different background components.

background sample (continuum events or  $B\bar{B}$  events). As a general criterion to choose the selection cuts we have maximized the figure of merit of significance  $S/\sqrt{S+B}$ , where  $S$  ( $B$ ) is the number of signal (background) events, favouring higher efficiency regions when the significance is almost constant as a function of the cut.

The  $K_S^0$  from the  $D^0$  is reconstructed from pairs of oppositely charged pions and its invariant mass is required to be within 9 MeV/ $c^2$  from the nominal  $K_S^0$  mass [7]. The requirement  $\cos \alpha_{K_S^0}(D^0) > 0.99$  where  $\alpha_{K_S^0}(D^0)$  is the angle between the  $K_S^0$  line of flight (line between the  $D^0$  vertex and the  $K_S^0$  vertex) and its momentum (constructed with the two pions momentum), is particularly helpful in removing the background from  $D^0 \rightarrow 4\pi$ . (See Figure 2 of [4]).

The  $D^0$  is selected by combining  $K_S^0$  candidates with two oppositely charged pions and requiring its invariant mass to be within 12 MeV/ $c^2$  from the nominal mass. A kinematic mass constraint is applied on  $D^0$  (via **TreeFitter** algorithm) improving the  $D^0$  energy estimation and therefore the  $\Delta E$  resolution (see Table 3). All along the analysis we use the  $D^0$  raw mass (without mass constraint) for selection cuts and for the true  $D^0$  extraction, as explained in the next sections.<sup>2</sup>

	TreeFitter $D^0$ mass constraint	Tree Fitter NO $D^0$ mass constraint	GeoKin $D^0$ mass constraint
$\Delta E$ resolution (MeV)	$10.8 \pm 0.3$	$13.0 \pm 0.8$	$11.0 \pm 0.3$

Table 3: Results from the gaussian fit of the  $\Delta E$  distribution on signal Monte Carlo sample.

We have required the  $D^0$  and  $B$  vertex fit to have converged (referred to as “ $P[\chi^2(D^0/B)_{vtx}, ndof] > 0$ ” in the following). This is a very conservative cut that rejects a small number of badly reconstructed background events.

Identical selection criteria to the  $K_S^0$  from the  $D^0$  have been applied to the  $K_S^0$  from the  $K^*$ . They have very similar invariant mass resolutions as reported in Table 4. It’s also required that  $\cos \alpha_{K_S^0}(K^*) > 0.99$  where  $\alpha_{K_S^0}(K^*)$  is the angle between the  $K_S^0$  direction of flight (line between the  $B$  vertex and the  $K_S^0$  vertex - the  $B$  vertex corresponds to the  $K^*$  vertex) and its momentum. In this case, for example, background events coming from  $B^- \rightarrow D^0 a_1^- (a_1^- \rightarrow 3\pi)$  decay mode are furtherly suppressed after applying that cut.

We have also applied cuts on the invariant mass of the  $K^*$  and on the cosine of the helicity angle

<sup>2</sup>The improvement in  $\Delta E$  resolution is greater for the  $K^{*-} \rightarrow K^- \pi^0$  decay mode, that has been reconstructed for a later study.

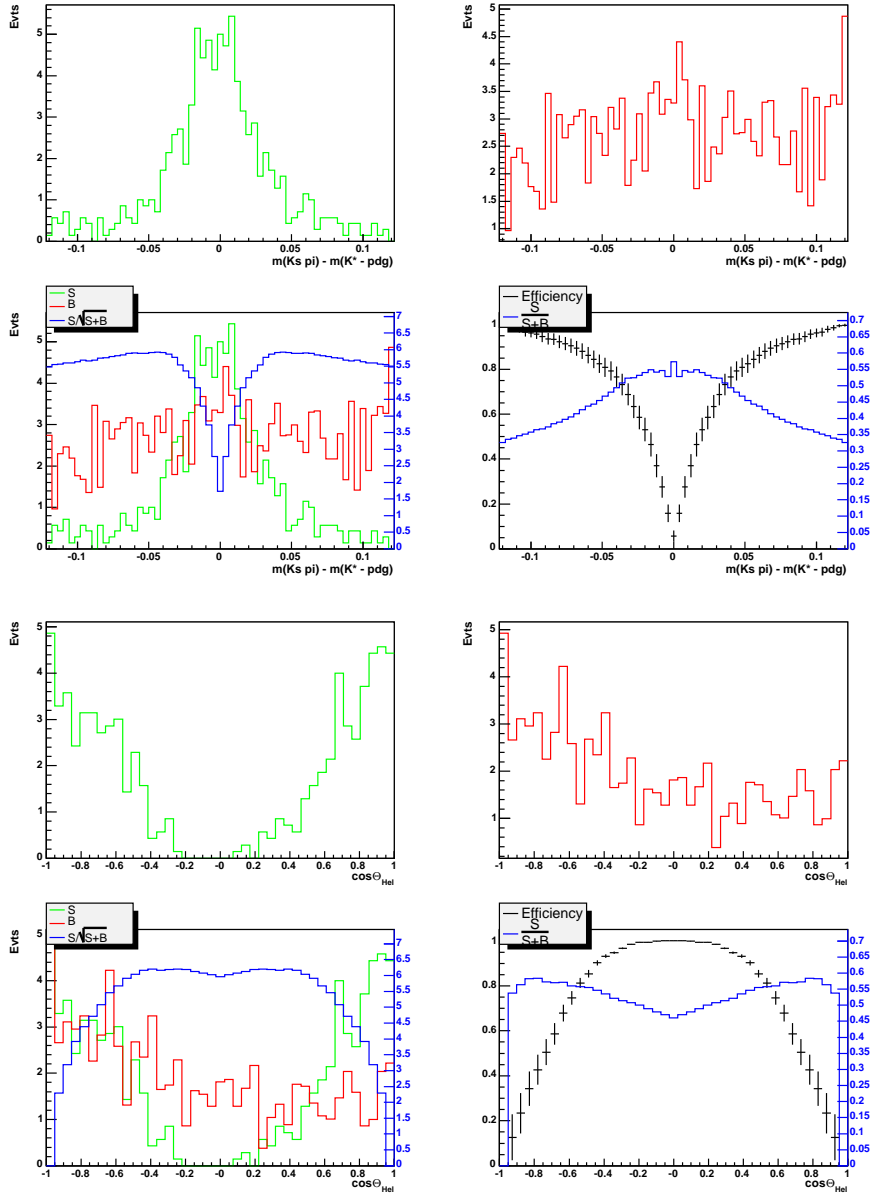


Figure 1: In the top-left plot (green) we show the distribution of the variable for the signal. In the top-right plot the variable distribution for the background. In bottom-left the significance as a function of the cut on the selected variable and in bottom-right the purity (histogram) and the efficiency (point with error bars) as a function of the cut. (Top 4 plots) Sequence of plot described above for the invariant mass of the  $K^{*-}$ . (Bottom 4 plots) Same plots for  $\cos \theta_{\text{Hel}}$  of the  $K^{*-}$  daughters.

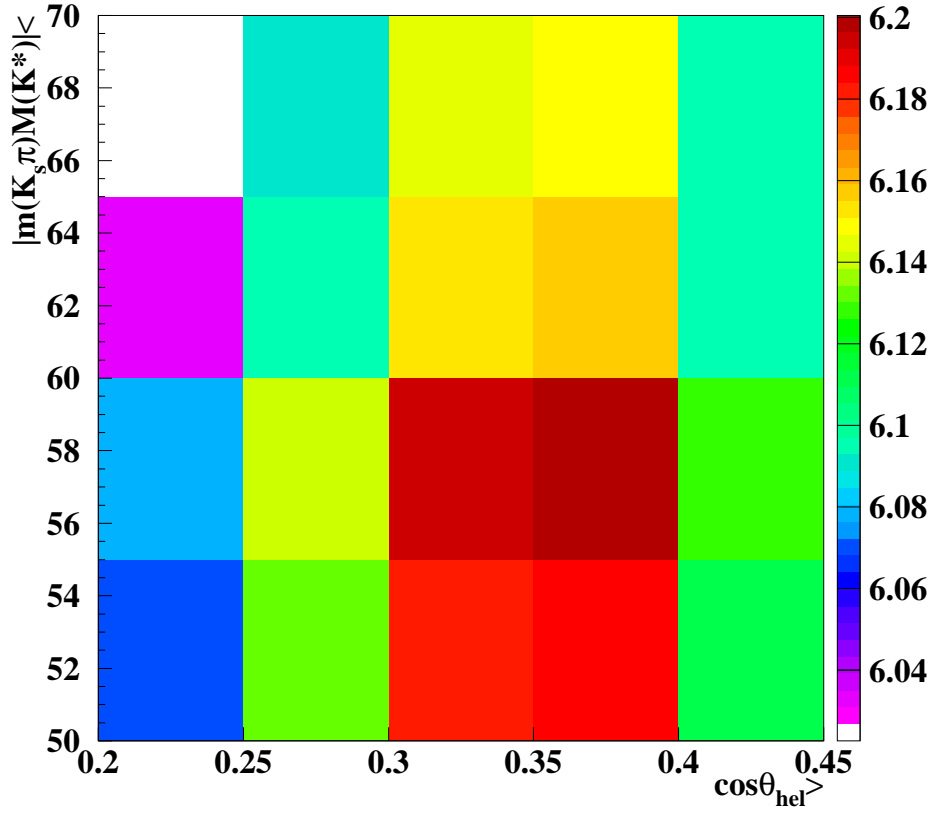


Figure 2: 2D plot of the significance with respect to the cut on the  $K^*$  mass and the cut on  $\cos \theta_{Hel}$ . The color scale represent the value of the significance, it increases from blue to red. The maximum value is 6.2 with  $|m_{K^*} - m_{K^*}(PDG)| < 55 \text{ MeV}/c^2$  and  $|\cos \theta_{Hel}| > 0.35$ .

Fitted mass of the $K_S^0$	from data sample	from MC sample
from the $D^0$	$497.9 \pm 0.1$ MeV	$498.3 \pm 0.1$ MeV
from the $K^*$	$497.7 \pm 0.1$ MeV	$498.3 \pm 0.1$ MeV
Fitted width of the $K_S^0$	from data sample	from MC sample
from the $D^0$	$2.41 \pm 0.05$ MeV	$2.30 \pm 0.11$ MeV
from the $K^*$	$2.26 \pm 0.05$ MeV	$2.20 \pm 0.10$ MeV

Table 4: *Results from the gaussian fit of the  $K_S^0$  mass distribution on data and Monte Carlo samples.*

of the  $K^*$  daughters,  $\cos \theta_{Hel}$  (see Figure 1). The helicity angle  $\theta_{Hel}$  is defined as the angle in the  $K^*$  rest frame between the direction of flight of a  $K^*$  daughter with respect to the direction of flight of the  $K^*$  in the  $B$  rest frame. As a cross check, we also plot the significance variation depending on the  $K^*$  mass cut and the cosine of the helicity cut (See Figure 2). This plot is in agreement with the previous ones, so we decide to fix the cut as it follows :  $|m_{K^*} - m_{K^*}(PDG)| < 55$  MeV/ $c^2$  and  $|\cos \theta_{Hel}| > 0.35$ . The  $K^*$  has spin 1, therefore the angular distribution is a function of the helicity angle,  $\frac{dN}{d(\cos \theta_{Hel})} \propto \cos^2 \theta_{Hel}$ . The distribution for background events is rather flat. In order to be consistent with the definition of the Fisher discriminant used for the  $B^- \rightarrow D^{(*)0} K^-$  we have applied the same cut on  $|\cos \theta_T| < 0.8$ , where  $\theta_T$  is the angle between the thrust axis of the  $B$  and the thrust axis of the rest of the event.

The final selection criteria are :

- $|m_{K_S^0}(D^0) - m_{K_S^0}(PDG)| < 9$  MeV/ $c^2$
- $|m_{K_S^0}(K^*) - m_{K_S^0}(PDG)| < 9$  MeV/ $c^2$
- $|m_{D^0} - m_{D^0}(PDG)| < 12$  MeV/ $c^2$
- $|\cos \theta_T| < 0.8$
- $P(\chi^2, D^0) > 0$
- $P(\chi^2, B) > 0$
- $\cos \alpha_{K_S^0}(D^0) > 0.99$
- $\cos \alpha_{K_S^0}(K^*) > 0.99$
- $|m_{K^*} - m_{K^*}(PDG)| < 55$  MeV/ $c^2$
- $|\cos \theta_{Hel}| > 0.35$
- $|\Delta E| < 25$  MeV
- $m_{ES} > 5.2$  MeV/ $c^2$

The overall reconstruction efficiency for signal events is  $\epsilon_{sig} = (11.1 \pm 0.5)\%$  after all selection criteria are applied. The significance of the signal in the final signal region  $|\Delta E| < 25$  MeV and  $m_{ES} > 5.270$  GeV/ $c^2$  is  $S/\sqrt{S+B} = 6.2$ . Table 5 shows the step by step efficiencies for data and the different Monte Carlo samples.

	signal (%)	$B^+B^-$	$B^0B^0$	$uds$	$c\bar{c}$	$\frac{S}{\sqrt{S+B}}$	$\frac{S}{S+B}$
After reconstruction	$23.8 \pm 0.6$	$(4.36 \pm 0.03)10^{-5}$	$(4.46 \pm 0.03)10^{-5}$	$(4.04 \pm 0.02)10^{-5}$	$(11.21 \pm 0.05)10^{-5}$	1.69	0.02
$ \cos(\theta_T)  < 0.8$	$17.7 \pm 0.6$	$(2.89 \pm 0.02)10^{-5}$	$(2.89 \pm 0.02)10^{-5}$	$(8.6 \pm 0.1)10^{-6}$	$(2.30 \pm 0.02)10^{-5}$	2.33	0.05
$m_{K_S^0}^{D^0}$ window $< 0.009$	$17.0 \pm 0.6$	$(2.14 \pm 0.02)10^{-5}$	$(2.06 \pm 0.02)10^{-5}$	$(6.0 \pm 0.1)10^{-6}$	$(1.68 \pm 0.02)10^{-5}$	2.63	0.07
$P(\chi^2, D^0) > 0$	$17.0 \pm 0.6$	$(2.14 \pm 0.02)10^{-5}$	$(2.06 \pm 0.02)10^{-5}$	$(6.0 \pm 0.1)10^{-6}$	$(1.68 \pm 0.02)10^{-5}$	2.63	0.07
$\cos \alpha_{K_S^0}^{D^0} > 0.99$	$16.4 \pm 0.6$	$(1.21 \pm 0.01)10^{-5}$	$(1.05 \pm 0.01)10^{-5}$	$(3.0 \pm 0.1)10^{-6}$	$(1.02 \pm 0.02)10^{-5}$	3.29	0.11
$m_{D^0}$ window $< 0.012$	$15.2 \pm 0.5$	$(7.3 \pm 0.1)10^{-6}$	$(4.5 \pm 0.1)10^{-6}$	$(1.07 \pm 0.04)10^{-6}$	$(4.6 \pm 0.1)10^{-6}$	4.25	0.19
$m_{K_S^0}^{K^*}$ window $< 0.009$	$14.7 \pm 0.5$	$(5.0 \pm 0.1)10^{-6}$	$(3.2 \pm 0.1)10^{-6}$	$(7.7 \pm 0.3)10^{-7}$	$(3.3 \pm 0.1)10^{-6}$	4.84	0.25
$\cos \alpha_{K_S^0}^{K^*} > 0.99$	$14.5 \pm 0.5$	$(3.00 \pm 0.07)10^{-6}$	$(1.9 \pm 0.1)10^{-6}$	$(4.9 \pm 0.3)10^{-7}$	$(2.4 \pm 0.1)10^{-6}$	5.61	0.34
$P(\chi^2, B) > 0$	$14.5 \pm 0.5$	$(3.00 \pm 0.07)10^{-6}$	$(1.9 \pm 0.1)10^{-6}$	$(4.9 \pm 0.3)10^{-7}$	$(2.4 \pm 0.1)10^{-6}$	5.61	0.34
$m_{K^*}$ window $< 0.055$	$12.2 \pm 0.5$	$(1.53 \pm 0.05)10^{-6}$	$(0.94 \pm 0.04)10^{-6}$	$(2.6 \pm 0.2)10^{-7}$	$(1.13 \pm 0.05)10^{-6}$	6.00	0.47
$ \cos(\theta_{hel})  > 0.35$	$11.6 \pm 0.5$	$(1.11 \pm 0.04)10^{-6}$	$(0.74 \pm 0.04)10^{-6}$	$(1.8 \pm 0.2)10^{-7}$	$(7.5 \pm 0.4)10^{-7}$	6.22	0.53
$ \Delta E  < 0.025$	$11.1 \pm 0.5$	$(1.2 \pm 0.2)10^{-7}$	$(0.8 \pm 0.1)10^{-7}$	$(0.18 \pm 0.05)10^{-7}$	$(1.2 \pm 0.2)10^{-7}$	-	-

Table 5: Efficiency (ratio of fully matched combinations over total number of signal events) and background rejection rates (number of combinations over total number of background events for each sample) after each cut, with  $m_{ES} > 5.2$ . Binomial errors are reported. Purity and significance in the signal box region ( $m_{ES} > 5.270 \text{ GeV}/c^2$  and  $|\Delta E| < 0.025 \text{ GeV}$ ).

### 1.3 Background characterization

The most relevant source of background comes from the *continuum* events.<sup>3</sup> Those events are suppressed with the cut on  $|\cos\theta_T| < 0.8$  and with the use of the Fisher discriminant in the  $CP$  likelihood fit, see Section 3. The fraction of continuum events,  $f_{\text{Cont}} = \frac{N_{\text{Cont}}}{N}$ , after all the cuts applied in the region  $m_{ES} > 5.2 \text{ GeV}/c^2$  is  $f_{\text{Cont,mc}} = 0.60 \pm 0.02$  from Monte Carlo simulation counting.<sup>4</sup> From the fit on data we find  $f_{\text{Cont,data}} = 0.74 \pm 0.07$ , see yield in Table 13. The  $B\bar{B}$  events have similar event shape distribution to the signal and they have been suppressed with a tight cut on  $|\Delta E| < 25 \text{ MeV}$ .

The  $B^- \rightarrow D^0 K^{*-}$  decay mode has potential sources of *physical background*<sup>5</sup>, hard to suppress. The final state we are considering is:

$$D^0 K^{*-} = [(\pi^+ \pi^-)_{K_S^0} \pi^+ \pi^-]_{D^0} \quad [(\pi^+ \pi^-)_{K_S^0} \pi^-]_{K^{*-}}$$

The following decay modes have been studied on Monte Carlo simulation and we concluded they are negligible with the current statistics:

- $D_{4\pi}^0 K^{*-}$ : this decay mode with a relatively smaller branching ratio wrt to the signal,  $Br(D^0 \rightarrow 4\pi) = (7.3 \pm 0.5) \cdot 10^{-3}$ . The contribution of this decay mode is negligible after we apply all the selection criteria. Relevant for the suppression of this background is the cut on  $\cos \alpha_{K_S^0}^{D^0} > 0.99$ .
- $K_S^0 K_S^0 K^{*-}$ : the branching ratio of this decay mode is not reported on the PDG. It is present in the Monte Carlo  $B\bar{B}$  events and its contribution is negligible after all cuts. No events have been found on  $\simeq 1 \text{ ab}^{-1} B\bar{B}$  Monte Carlo sample where the decay mode was generated assuming  $Br(B^0 \rightarrow K^0 \bar{K}^0 K^{*-}) = 10^{-5}$ . We have searched on data for the evidence of this background considering the  $D^0$  sidebands, (*i.e.*  $|m_D^0 - m_{PDG}| > 20 \text{ MeV}/c^2$ ), and fitting the  $m_{ES}$  distribution after all the selection criteria applied. In Figure 3 we show there is no statistical evidence of such a signal. It is worth noting that the  $D^0$  invariant mass region considered in the  $m_{ES}$  fit is almost 5 times greater compared to the one of the  $B^- \rightarrow D^0 K^{*-}$  signal region.

<sup>3</sup>With continuum events we refer to  $e^+e^- \rightarrow q\bar{q}$  events, where  $q = u, d, s, c$  quarks.

<sup>4</sup>This estimate depends on the  $Br$  we assume for the signal events.

<sup>5</sup>We refer with physical background to decay modes with identical final state particles to the signal.

- $D^0\pi^-\pi^+\pi^-$ : this decay mode has a relatively large branching ratio  $Br(B^- \rightarrow D^0\pi^-\pi^+\pi^-) = (1.1 \pm 0.4)\%$  and it includes  $Br(B^- \rightarrow D^0a_1^-) = (6.0 \pm 3.3) \cdot 10^{-3}$ . We find 3 events of this decay mode on  $\simeq 1\text{ab}^{-1} B\bar{B}$  Monte Carlo sample. We neglect this contribution in the  $\Delta E$  parameterization of the background. We assume a linear distribution in  $\Delta E$  for  $B\bar{B}$  events.
- $D^0K_s^0\pi^-$ : this is identical final state to the signal but the  $(K_s^0\pi^-)$  system is decaying with relative angular momentum  $L=0$  instead of  $L=1$ . These events are considered actually as signal events in the  $CP$  likelihood fit as they reach the final state through  $b \rightarrow u$  and  $b \rightarrow c$  interfering amplitudes. We will refer in the following to those events as *signal Non-Resonant*. It has been shown in [8, 9] that signal Non-Resonant has a relative contribution of  $< 5\%$  respect to the  $D^0K^{*-}$ , in another  $B^- \rightarrow D^0K^{*-}$  analysis with very similar cuts applied.

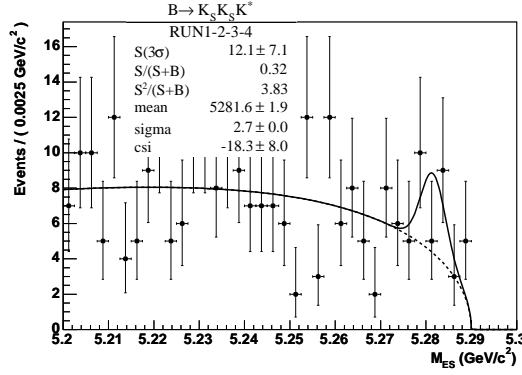


Figure 3: *Unbinned maximum Likelihood fit to the  $m_{ES}$  distribution doesn't show any evidence of  $K_s^0K_s^0K^{*-}$  signal events on the  $D^0$  sidebands after all the selection cuts are applied.*

As in the  $B^- \rightarrow D^{(*)0}K^-$  analysis, we divide the background events in true  $D^0$  and false  $D^0$  in order to characterize the Dalitz shape. The estimate of the fraction of true  $D^0$  ( $R$ ), has been done on Monte Carlo events by counting. The values are reported in Table 6, together with the fraction of right-sign  $D^0$ ,  $R^{RS} = \frac{N_{D^0h^{*-}}}{N_{D^0h^{*-}} + N_{\bar{D}^0h^{*-}}}$  where  $h^{*-}$  is a candidate  $K^{*-}$ . The fraction of  $R^{RS}$  is evaluated requiring the Monte Carlo truth match of the  $D^0$  and the lundId of the  $D^0$ . Then we count the number of true  $D^0$  and  $\bar{D}^0$  candidate associated with an  $h^{*-}$  to take into account an eventual charge-flavor correlation.

Fraction	Estimate from generic MC	Estimate from data
$R_{\text{Cont}}$ (real $D^0$ 's in Cont)	$0.21 \pm 0.02$	$0.20 \pm 0.06$
$R_{\text{B}\bar{\text{B}}}$ (real $D^0$ 's in $B\bar{B}$ )	$0.18 \pm 0.02$	$0.20 \pm 0.06$
$R_{\text{Cont}}^{RS}$ ( $D^0 K^{*-}$ in Cont)	$0.51 \pm 0.06$	-
$R_{\text{B}\bar{\text{B}}}^{RS}$ ( $D^0 K^{*-}$ in $B\bar{B}$ )	$0.67 \pm 0.06$	-

Table 6:  *$D^0$  fractions for background events are estimated from generic MC and data, for the region  $|\Delta E| < 25$  MeV and  $m_{ES} > 5.2$  GeV/ $c^2$ . In data we have restricted the  $m_{ES}$  region to  $5.2 < m_{ES} < 5.27$  GeV/ $c^2$  to exclude the signal events.*

The fractions of true  $D^0$  have been evaluated also on data considering the  $m_{ES}$  sidebands. The fraction can be extracted from a fit to the  $D^0$  invariant mass using as PDF, a gaussian for the

$D^0$  signal plus a constant for the background. Due to the small statistics we fixed the mean of the gaussian to  $\mu_{D^0} = 1864.5 \text{ MeV}/c^2$  and the width to  $\sigma_{D^0} = 6.0 \text{ MeV}/c^2$  from signal Monte Carlo fitted values. Being the fraction of true  $D^0$  identical, within the errors, for  $B\bar{B}$  and continuum events on Monte Carlo, we have assumed the fractions to be identical also on data. In figure 4 it is shown the fit to the  $D^0$  invariant mass distribution for data (left plot) and for Monte Carlo events (right plot).

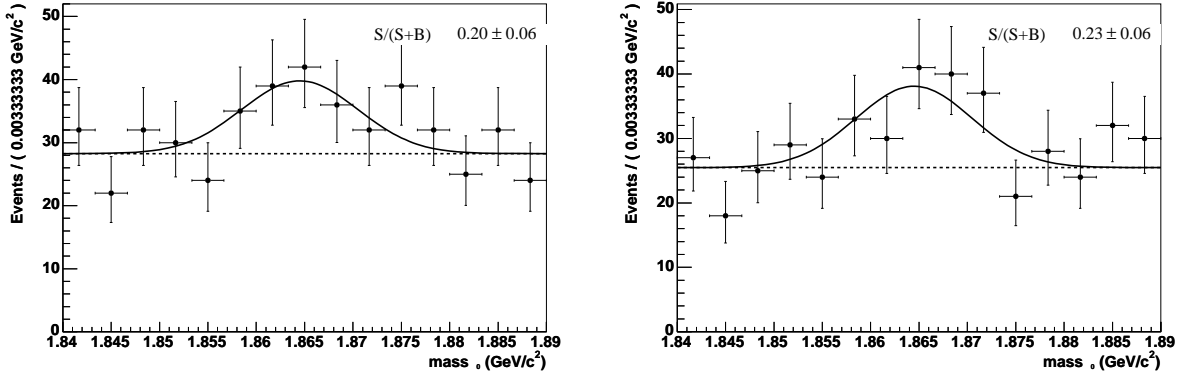


Figure 4: The fit to the  $D^0$  distribution shows evidence of true  $D^0$  background events. The events are selected in the  $m_{ES}$  sidebands ( $m_{ES} < 5.27 \text{ GeV}/c^2$ ) with all the selection cuts applied. Left: data; Right: Monte Carlo

#### 1.4 Best candidate choice

In the fit for the extraction of the  $CP$  parameters we select one  $B$  candidate per event. The best candidate (per event) is chosen according to the minimum value of the  $\chi^2 = \chi^2(m_{D^0}, m_{K^*})$ :

$$\chi^2(m_{D^0}, m_{K^*}) = \frac{(m_{D^0} - m_{D^0,PDG})^2}{\sigma_{D^0}^2} + \frac{(m_{K^*} - m_{K^*,PDG})^2}{\sigma_{K^*}^2 + \Gamma_{K^*}^2}$$

where  $\sigma$  is the experimental resolution on Monte Carlo signal events and  $\Gamma_{K^*}$  is the intrinsic width of the  $K^*$ .

The multiplicity of candidates on data in the signal region ( $m_{ES} > 5.270 \text{ MeV}/c^2$ ,  $|\Delta E| < 25 \text{ MeV}$ ) after all the cuts is  $N_{cand} = 1.055 \pm 0.005$ , see Figure 5. The efficiency of the best candidate choice for signal events is approximately  $\epsilon_{best} = 75\%$ , evaluated on Monte Carlo signal events.

#### 1.5 Data/Monte Carlo comparison

We produced plots for the relevant variables used in the analysis to compare data and MC samples after all cuts are applied but the one on the plotted variable. The colored histograms represent the different Monte Carlo component and the points represent the data. Each component is normalized to  $208.4 \text{ fb}^{-1}$ , the luminosity of the On-peak data. By visual comparison a satisfactory data/simulation agreement comes out. It's worth noting the shift in the  $m_{ES}$  distribution, that can be quantified as  $\Delta m_{ES} = 1.7 \text{ MeV}/c^2$ .

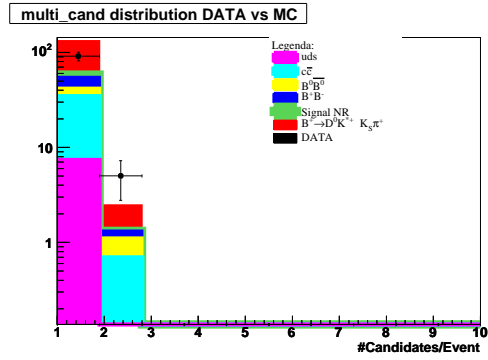


Figure 5: *Distribution of the number of  $B$  candidates per event after all the cuts applied in the signal region  $m_{ES} > 5.270 \text{ MeV}/c^2$ ,  $|\Delta E| < 25 \text{ MeV}$ . Colored histograms represent background events and point with error bars represent data.*

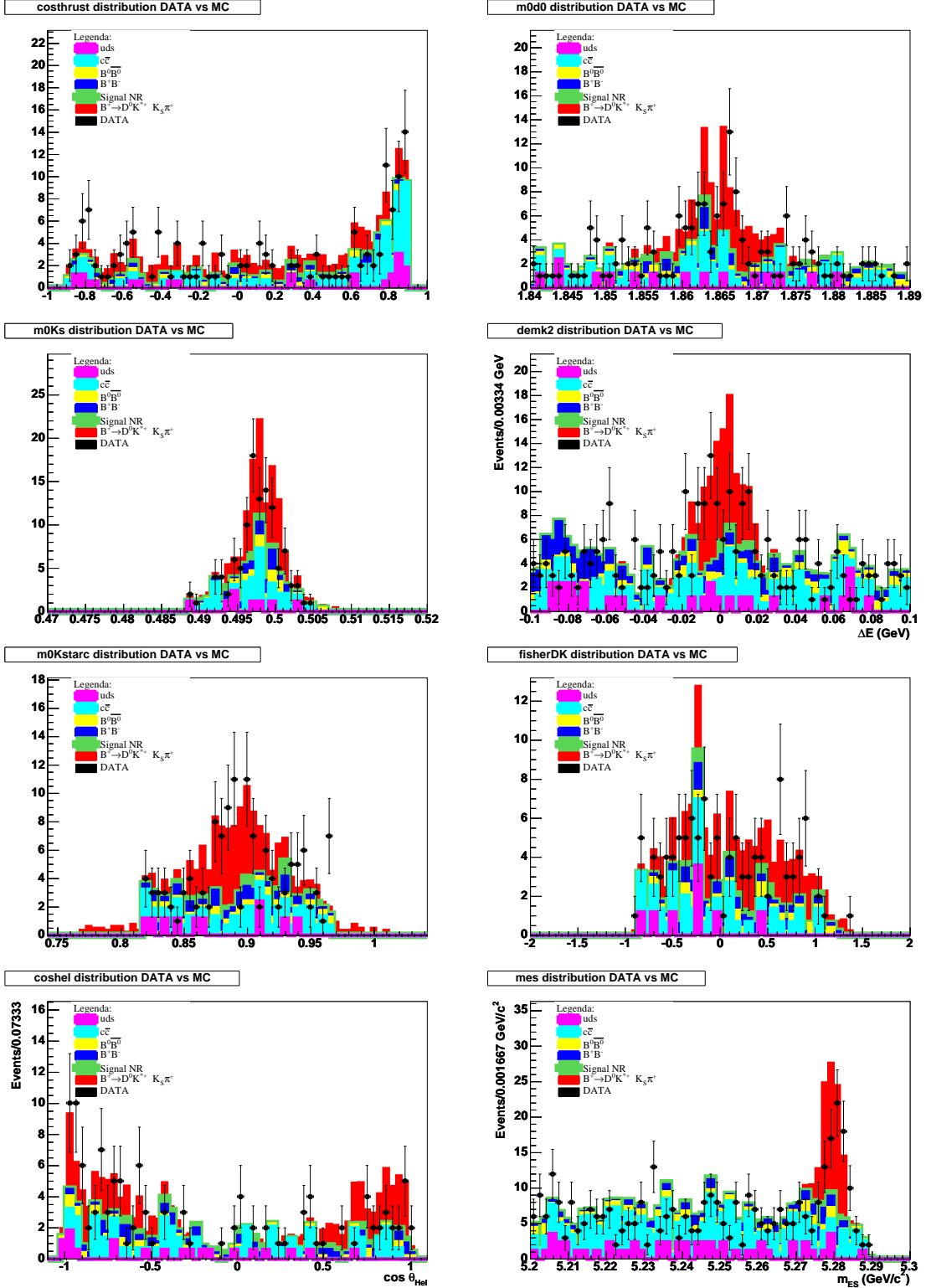


Figure 6: The plots show the data/MC comparison for the relevant variables used in the selection criteria. From the top left to the bottom right the following quantities are reported:  $\cos(\theta_T)$ ,  $D^0$  mass,  $K_S^0$  mass,  $\Delta E$ ,  $K^*$  mass, Fisher,  $\cos\theta_{Hel}$ ,  $m_{ES}$ . The events in the plots are selected applying all the selection criteria but the one on the displayed variable.

## 2 PDF for $B^- \rightarrow D^0 K^{*-}$ decays

Compared to  $B^- \rightarrow D^{(*)0} K^-$ ,  $B^- \rightarrow D^0 K^{*-}$  decays are affected by an additional difficulty, consequence of the fact that the natural width of the  $K^{*-}$  is not small ( $\sim 50$  MeV) and the interference with the non-resonant  $B^- \rightarrow D^0 (K\pi)_{\text{non-}K^*}^-$  processes may not be negligible. This changes the relationships between the unitarity angle  $\gamma$  and the experimental observables.

Let's write the amplitudes of the  $B^- \rightarrow (D^0 X_s^-)_p$  and  $B^- \rightarrow (\bar{D}^0 X_s^-)_p$  processes, where  $p$  indicates a point in the phase space of the final state and  $X_s^-$  is a state with strangeness, as:

$$A(B^- \rightarrow (D^0 X_s^-)_p) = A_{cp} e^{i\delta_{cp}} \quad (1)$$

$$A(B^- \rightarrow (\bar{D}^0 X_s^-)_p) = A_{up} e^{i\delta_{up}} e^{-i\gamma} \quad (2)$$

$$A(D^0 \rightarrow f) = A_f e^{i\delta_f} \quad (3)$$

$$A(D^0 \rightarrow \bar{f}) = A_{\bar{f}} e^{i\delta_{\bar{f}}}, \quad (4)$$

where  $A_{cp}$ ,  $A_{up}$ ,  $A_f$  and  $A_{\bar{f}}$  are real and positive. The index  $p$  indicates the position in the phase space of  $DX_s^-$ , that is,  $A_c$ ,  $A_u$ ,  $\delta_c$  and  $\delta_u$  generally vary as a function of  $p$ . The subscript  $c$  and  $u$  refer to the  $b \rightarrow c$  and  $b \rightarrow u$  transitions, respectively. The amplitudes  $A_{cp} e^{i\delta_{cp}}$  and  $A_{up} e^{i\delta_{up}} e^{-i\gamma}$  generally include both the resonant  $B^- \rightarrow D^0/\bar{D}^0 K^{*-}$  processes and the non-resonant contributions. The amplitudes for the  $D^0$  decay can generally include the case where  $D^0 \rightarrow 3$ -body, for instance  $D^0 \rightarrow K_S^0 \pi^- \pi^+$ ; in this case  $A_f e^{i\delta_f} = f(m_+^2, m_+^2)$  and  $A_{\bar{f}} e^{i\delta_{\bar{f}}} = f(m_+^2, m_-^2)$ , that is,  $A_f$ ,  $A_{\bar{f}}$ ,  $\delta_f$  and  $\delta_{\bar{f}}$  are functions of the Dalitz plot coordinates  $m_{\pm}^2$ , where  $m_-^2$  and  $m_+^2$  are the squared masses of the  $K_S^0 \pi^-$  and  $K_S^0 \pi^+$  combinations.

The amplitude of the process  $B^- \rightarrow D[\rightarrow f]X_s^-$  can be written as

$$A(B^- \rightarrow (D[\rightarrow f]X_s^-)_p) = A_{cp} A_f e^{i(\delta_{cp} + \delta_f)} + A_{up} A_{\bar{f}} e^{i(\delta_{up} + \delta_{\bar{f}} - \gamma)}. \quad (5)$$

From Eq. (5) the rate of the process  $B^- \rightarrow D[\rightarrow f]X_s^-$  is

$$\Gamma(B^- \rightarrow D[\rightarrow f]X_s^-) = \int dp \left( A_{cp}^2 A_f^2 + A_{up}^2 A_{\bar{f}}^2 + 2A_{cp} A_f A_{up} A_{\bar{f}} \text{Re}(e^{i(\delta_p + \delta_D - \gamma)}) \right), \quad (6)$$

where  $\delta_p = \delta_{up} - \delta_{cp}$  and  $\delta_D = \delta_{\bar{f}} - \delta_f$ . The rate for the charge-conjugated mode is the one in Eq. (6) with  $\gamma \rightarrow -\gamma$ . Analogously, the partial rates  $\Gamma(B^- \rightarrow D^0 X_s^-)$  and  $\Gamma(B^- \rightarrow \bar{D}^0 X_s^-)$  are

$$\Gamma(B^- \rightarrow D^0 X_s^-) = \int dp A_{cp}^2, \quad (7)$$

$$\Gamma(B^- \rightarrow \bar{D}^0 X_s^-) = \int dp A_{up}^2. \quad (8)$$

Following the same notation as in [10], we introduce the quantities  $r_s$ ,  $k$  and  $\delta_s$ , that will be useful in the following sections:

$$r_s^2 = \frac{\Gamma(B^- \rightarrow \bar{D}^0 X_s^-)}{\Gamma(B^- \rightarrow D^0 X_s^-)} = \frac{\int dp A_{up}^2}{\int dp A_{cp}^2}, \quad (9)$$

$$k e^{i\delta_s} = \frac{\int dp A_{cp} A_{up} e^{i\delta_p}}{\sqrt{\int dp A_{cp}^2 \int dp A_{up}^2}}, \quad (10)$$

where  $0 \leq k \leq 1$  for the Schwartz inequality and  $\delta_s \in [0, 2\pi]$ . In the limit of a  $B \rightarrow 2$ -body decay, such as  $B^- \rightarrow DK^-$ , we have:

$$r_s \rightarrow r_B \equiv \frac{|A(B^- \rightarrow \bar{D}^0 K^-)|}{|A(B^- \rightarrow D^0 K^-)|},$$

$$\delta_s \rightarrow \delta_B \equiv \text{strong phase of } \frac{A(B^- \rightarrow \bar{D}^0 K^-)}{A(B^- \rightarrow D^0 K^-)}, \quad (11)$$

$$k \rightarrow 1.$$

In the case of the  $D^0 \rightarrow K_S^0 \pi^+ \pi^-$  decay,  $A_f e^{i\delta_f} = f(m_-^2, m_+^2)$  and  $A_{\bar{f}} e^{i\delta_{\bar{f}}} = f(m_+^2, m_-^2)$ . The amplitude for the process  $B^\mp \rightarrow D[-\rightarrow K_S^0 \pi^- \pi^+] X_s^\mp$  can be written as

$$A(B^\mp \rightarrow D[-\rightarrow K_S^0 \pi^- \pi^+] X_s^\mp) = A_{cp} e^{i\delta_{cp}} f(m_\mp^2, m_\pm^2) + A_{up} e^{i\delta_{up} \mp \gamma} f(m_\pm^2, m_\mp^2), \quad (12)$$

and the rate is

$$\begin{aligned} \Gamma(B^\mp \rightarrow D[-\rightarrow K_S^0 \pi^- \pi^+] X_s^\mp) &\propto |f_\mp|^2 + r_s^2 |f_\pm|^2 + \\ &2kr_s \{ \cos(\delta_s \mp \gamma) \text{Re}[f_\mp f_\pm^*] + \sin(\delta_s \mp \gamma) \text{Im}[f_\mp f_\pm^*] \} \\ &\equiv |f_\mp|^2 + r_s^2 |f_\pm|^2 + \\ &2kr_s |f_\mp| |f_\pm| \cos(\delta_s + \delta_D(m_\mp^2, m_\pm^2) \mp \gamma), \end{aligned} \quad (13)$$

where  $\delta_D(m_\mp^2, m_\pm^2)$  is the strong phase difference between  $f(m_\pm^2, m_\mp^2)$  and  $f(m_\mp^2, m_\pm^2)$  and  $r_s$ ,  $k$  and  $\delta_s$  are defined in Eqs. (9) and (10). We have simplified the notation using  $f_\pm \equiv f(m_\pm^2, m_\mp^2)$  and  $f_\mp \equiv f(m_\mp^2, m_\pm^2)$ . Let us stress that the parameterization given in Eq. (13) includes both resonant and non-resonant  $(K\pi)^\mp$  contributions, since the amplitudes in Eqs. (1) and (2) include both. The effective (and general) parameterization given in Eq. (13) can be rewritten in terms of the cartesian coordinates

$$\begin{aligned} x_{s\pm} &= \text{Re}[kr_s e^{i(\delta_s \pm \gamma)}], \\ y_{s\pm} &= \text{Im}[kr_s e^{i(\delta_s \pm \gamma)}], \end{aligned} \quad (14)$$

as

$$\Gamma(B^\mp \rightarrow D[-\rightarrow K_S^0 \pi^- \pi^+] X_s^\mp) \propto |f_\mp|^2 + r_s^2 |f_\pm|^2 + 2 [x_{s\mp} \text{Re}[f_\mp f_\pm^*] + y_{s\mp} \text{Im}[f_\mp f_\pm^*]]. \quad (15)$$

The functional form of the PDF in eq. 15 doesn't change when the reconstruction efficiency is not uniform over the  $B$  phase space, as it's explained in the appendix B.

The measurement of  $\gamma$  in this analysis is performed by extracting the terms proportional to  $r_s^2$  and proportional to  $kr_s$  independently. It is done by using Eq. (15) and fitting simultaneously for  $x_{s\mp}$ ,  $y_{s\mp}$  and  $r_s^2$ . Since the experimental sensitivity to  $\gamma$  comes from the interference term, linear in  $r_s$ , we expect the effect of floating the  $r_s^2$  factor to be quite small (as the terms quadratic in  $r_s$  are suppressed for  $r_s$  relatively small), as shown in section 3.4. This provides an easy way to extract directly the effective cartesian coordinates from data without any assumption about the non-resonant contribution and its interference with the resonant signal, with the additional advantage that both resonant and non-resonant decays contribute coherently to the sensitivity to  $\gamma$ . Toy Monte Carlo studies have proven the feasibility of this procedure for the current data sample, as described section 3.4. Thus with this method no systematic uncertainty is required to be assigned due to the presence of  $B^- \rightarrow D(K\pi)_{\text{non-}K^*}^-$  decays.

Let us note that this method to account for non-resonant decays is different and significantly more powerful than that used by Belle in their preliminary measurement using  $B^- \rightarrow D^0 K^{*-}$  decays [11]. There the non-resonant contribution is neglected in the signal PDF and considered as background. Belle evaluates the systematic uncertainty due to this effect to be  $8^\circ$ . The estimate has been done by generating pseudo experiments with  $D^0$  Dalitz distributions as the result of the

signal resonant plus a coherent non-resonant contribution and varying the parameters of the non-resonant component within conservative ranges. The systematic uncertainty has been evaluated from the consequent variation of the  $B^- \rightarrow D^0 K^{*-}$   $CP$  parameters, whose range of variation is not provided in the paper.

### 3 $CP$ fit

The general log-likelihood function and fit strategy used to extract the  $CP$  parameters is identical to that used for  $B^- \rightarrow D^{(*)0} K^-$  events, as described in section 6 of Ref. [4]. Based on the background characterization of section 1, we consider four different components in the probability density function (PDF): signal (Sig), wrong sign signal (SigWS), continuum (Cont) and  $B\bar{B}$  ( $B\bar{B}$ ).

The wrong sign signal component corresponds to real signal events where the charge of the  $K^*$  is opposite to that of the  $B$  meson due to a combinatorial wrong sign pion from the other  $B$  decay (i.e. the  $D^0$  is seen as  $\bar{D}^0$ ). These are potentially very dangerous events since they are  $CP$ -violating (as signal) but are with opposite sign.

The continuum background component is subdivided into two categories:

- fake (combinatorial)  $D^0$  (comb);
- real  $D^0$  ( $D^0$ ). Here we distinguish between real  $D^0$  mesons with a right sign (RS) random  $K^*$  (i.e.  $D^0 K^{*-}$  or  $\bar{D}^0 K^{*+}$ ) or a wrong sign (WS) random  $K^*$  (i.e.  $D^0 K^{*+}$  or  $\bar{D}^0 K^{*-}$ ). This splitting is needed in order to account for the misinterpretation of  $D^0$  decays as  $\bar{D}^0$  (and vice versa), relevant to parameterize correctly the Dalitz structure. This background component does not contain  $CP$ -violating effects.

The  $B\bar{B}$  component includes candidates with either a missing particle or a particle from the other  $B$  decay (like  $D^0(4\pi)K^{*+}$ ,  $D^0 a_1^+$ ,  $D^{0(*)}K^{(*)+}$  and  $D^0\eta\pi^+$ ), as well as events with a fake (combinatorial)  $D^0$ . This background type contains both non-peaking and peaking components (in  $m_{ES}$  and  $\Delta E$ ). This component is also split into two subtypes:

- real  $D^0$  ( $D^0$ ). As before, we distinguish between real  $D^0$  mesons with a right (RS) or a wrong sign (WS) random  $K^*$ . By default this category does not contain  $CP$  violation, but a set of  $CP$ -violating parameters has been introduced (by default fixed to zero) for systematic checks;
- combinatorial  $D^0$  (comb).

The PDF  $\mathcal{P}^\alpha$  can then be written as:

$$\begin{aligned} \mathcal{P}^\alpha = & f_{\text{Sig}}(1 - \kappa_{\text{SigWS}})\mathcal{P}_{\text{Sig}}^\alpha + f_{\text{Sig}}\kappa_{\text{SigWS}}\mathcal{P}_{\text{Sig}}^{\bar{\alpha}} + \\ & f_{\text{Cont}} \left\{ (1 - R_{\text{Cont}})\mathcal{P}_{\text{Cont}}^{\text{comb}} + R_{\text{Cont}} \left[ R_{\text{Cont}}^{\text{RS}}\mathcal{P}_{\text{Cont}}^\alpha + (1 - R_{\text{Cont}}^{\text{RS}})\mathcal{P}_{\text{Cont}}^{\bar{\alpha}} \right] \right\} + \\ & f_{\text{B}\bar{\text{B}}} \left\{ (1 - R_{\text{B}\bar{\text{B}}})\mathcal{P}_{\text{B}\bar{\text{B}}}^{\text{comb}} + R_{\text{B}\bar{\text{B}}} \left[ R_{\text{B}\bar{\text{B}}}^{\text{RS}}\mathcal{P}_{\text{B}\bar{\text{B}}}^\alpha + (1 - R_{\text{B}\bar{\text{B}}}^{\text{RS}})\mathcal{P}_{\text{B}\bar{\text{B}}}^{\bar{\alpha}} \right] \right\} \end{aligned} \quad (16)$$

where

- $\alpha = D^0, \bar{D}^0$ , and  $\bar{\alpha}$  denotes the  $CP$  conjugate state of  $\alpha$ ;
- $f_j$  is the fraction for component  $j = \text{Sig}, \text{Cont}, \text{B}\bar{\text{B}}$ ;
- $\kappa_{\text{SigWS}}$  is the fraction of wrong sign signal relative to (right sign) signal;
- $R_{\text{Cont}}$  ( $R_{\text{B}\bar{\text{B}}}$ ) is the fraction of real  $D^0/\bar{D}^0$  in Cont ( $\text{B}\bar{\text{B}}$ ) background component;
- $R_{\text{Cont}}^{\text{RS}}$  ( $R_{\text{B}\bar{\text{B}}}^{\text{RS}}$ ) is the fraction of right sign  $D^0/\bar{D}^0$  in Cont ( $\text{B}\bar{\text{B}}$ ) background component;

- $\mathcal{P}_j^\alpha$  is the PDF for component  $j$  and real  $D^0$  ( $\alpha = D^0$ ) or  $\bar{D}^0$  ( $\alpha = \bar{D}^0$ ), while  $\mathcal{P}_j^{\text{comb}}$  is the PDF for component  $j$  and fake  $D^0$ .  $\mathcal{P}_j^\alpha$  (and similarly  $\mathcal{P}_j^{\text{comb}}$ ) is parameterized as follows:

$$\mathcal{P}_j^\alpha \equiv \mathcal{P}_j^\alpha(m_{\text{ES}}) \mathcal{P}_j^\alpha(\mathcal{F}) \mathcal{P}_j^\alpha(m_+^2, m_-^2), \quad (17)$$

where  $\mathcal{P}_j^\alpha(m_+^2, m_-^2)$  is the Dalitz plot dependent part of the PDF, corrected by efficiency variations across the Dalitz plane,  $\epsilon(m_+^2, m_-^2)$ .  $\mathcal{P}_{\text{Sig}}^\alpha(m_+^2, m_-^2)$  is given by Eq. (15). In the current analysis we used an isobar model to parameterize the  $D^0 \rightarrow K_S^0 \pi^+ \pi^-$  Dalitz structure (described in Ref. [4]), while we use a K-matrix formalism [5] as alternative parameterization to estimate the Dalitz model uncertainty (section 5). A similar expression applies for fake  $D^0$ 's (comb), where  $\mathcal{P}_j^{\text{comb}}(m_+^2, m_-^2)$  can be estimated for  $j = \text{Cont}, \text{B}\bar{\text{B}}$  from Monte Carlo simulation, and for the case of Cont events can be compared to sideband and off-resonance data to assess the agreement between the simulation and the data.  $\mathcal{P}_j^\alpha(m_+^2, m_-^2)$  for  $j = \text{Sig}$  contains the  $CP$  violating terms (i.e. it is sensitive to the angle  $\gamma$ ), while  $\mathcal{P}_j^\alpha(m_+^2, m_-^2)$  for  $j = \text{Cont}, \text{B}\bar{\text{B}}$  and  $\mathcal{P}_j^{\text{comb}}(m_+^2, m_-^2)$  do not. An independent set of  $CP$ -violation parameters has been considered for  $j = \text{B}\bar{\text{B}}$  (by default fixed to zero) in order to study systematic errors induced by residual  $CP$  violating channels contributing to the  $\text{B}\bar{\text{B}}$  background. It has been verified that for the cuts used in the  $CP$  fit the correlations among the variables are either negligible or have no effect on the  $CP$  measurements. In particular, the correlation of Fisher with  $m_{\text{ES}}$  has been found to be negligible for all the background components (smaller than a few per cent). For signal it is at the level of 2.9% (see Fig. 7). The effect of this correlation has been verified to be completely negligible on all the  $CP$  parameters being measured in this analysis.

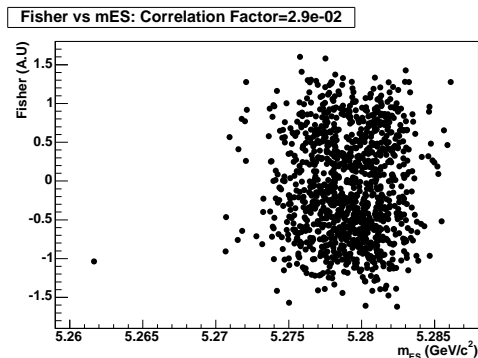


Figure 7: *Fisher- $m_{\text{ES}}$  correlation for  $B^- \rightarrow D^0 K^{*-}$  signal events. Even for background events the correlation was found to be negligible.*

Contrary to the  $B^- \rightarrow D^{(*)0} K^-$  analysis [4, 12], now we do not use  $\Delta E$  in the PDF, Eq. (17). This is motivated by two facts: i) we apply a signal only  $\Delta E$  cut ( $|\Delta E| < 25$  MeV); ii) there is no equivalent  $B^- \rightarrow D^{(*)0} \pi^-$  background in  $B^- \rightarrow D^0 K^{*-}$  events. Note that the main reason to use  $\Delta E$  in the PDF was to provide discrimination of remaining  $B^- \rightarrow D^{(*)0} \pi^-$  events in the  $B^- \rightarrow D^{(*)0} K^- \Delta E$  signal region. Moreover we do not have at hand a suitable control sample <sup>6</sup> from which we can fix the shapes of the  $\Delta E$  parameterization and the extraction from the  $B^- \rightarrow D^0 K^{*-}$  data themselves suffers the effects of a low statistics sample. The GLW and ADS  $B^- \rightarrow D^0 K^{*-}$  analysis [8, 9] relies also on  $m_{\text{ES}}$  only.

<sup>6</sup>One possibility we have considered is a  $B^- \rightarrow D^0 a_1^-$  sample but this is not yet available.

The extraction of the Sig, Cont and  $B\bar{B}$  component fractions, selection PDF shapes and  $CP$  parameters is performed using an extended unbinned likelihood function

$$\mathcal{L}_{ext} = \frac{e^{-\eta}\eta^N}{N!} \prod_{\alpha} \prod_{i=1}^{N_{\alpha}} \mathcal{P}^{\alpha}(i), \quad (18)$$

where  $\mathcal{P}^{\alpha}(i)$  is the total PDF given by Eq. (16) for event  $i$ . Here,  $N = N_{D^0} + N_{\bar{D}^0}$  is the total number of observed events, and  $\eta$  its expected value according to Poisson statistics. The normalization of the PDF is performed separately for  $B^+$  and  $B^-$  events and uses numerical integration dividing the Dalitz plot into a grid of  $N_{grid} \times N_{grid}$  cells, where typically  $N_{grid} = 200$ , which corresponds to 3.5 MeV precision on the  $K_S^0\pi^+$  and  $K_S^0\pi^-$  masses. Let us emphasize that Eq. 18 depends only on the  $D$  Dalitz variables since we integrated over the  $B$  Dalitz variables, as shown when obtaining Eq. 15. This the normalization of the PDF only requires integration over two Dalitz variables.

As in the case of the  $B^- \rightarrow D^{(*)0}K^-$  analysis [4, 12] the  $CP$  fit to the  $B^- \rightarrow D^0K^{*-}$  data is performed in two steps. First, the yields and PDF selection shapes are extracted from a combined fit to  $B^- \rightarrow D^0K^{*-}$  and  $B^- \rightarrow D^0\pi^-$  data, excluding the Dalitz information (i.e.  $\mathcal{P}_j^{\alpha}$  does not include  $\mathcal{P}_j^{\alpha}(m_+^2, m_-^2)$ ). Not all parameters can be extracted simultaneously from the  $B^- \rightarrow D^0K^{*-}$  data and some inputs are needed from either Monte Carlo or control samples, as described in section 3.1. Second, the Dalitz fit is performed fixing the selection PDF shapes to the values previously found and floating the yields and  $CP$  parameters.

### 3.1 Inputs

We describe in this section the inputs used in the  $CP$  fit.

#### 3.1.1 Selection PDF shapes

Figure 8 shows the  $m_{ES}$ ,  $\Delta E$ , and  $\mathcal{F}$  PDF shapes for Sig, Cont and  $B\bar{B}$  components, from generic Monte Carlo. The  $\Delta E$  PDF shapes are shown here but are not used in the  $CP$  fit, as described previously<sup>7</sup>. Only the  $m_{ES}$  PDF shapes for  $B\bar{B}$  are taken from the simulation, the others are either extracted from the fit to the  $B^- \rightarrow D^0K^{*-}$  data or from control samples. For  $m_{ES}$  we use a Gaussian for Sig, an Argus parameterization for Cont, and a Gaussian (with width fixed to 3.8 MeV/ $c^2$ ) plus an Argus function for  $B\bar{B}$ . The fraction of peaking background, defined as the fraction of the Gaussian peak with respect to all the  $B\bar{B}$  background (in  $m_{ES} > 5.2$  GeV/ $c^2$  region), is found to be  $(13.3 \pm 3.1)\%$ . The  $m_{ES}$  shape for Cont is assumed to be the same for  $B^- \rightarrow D^0K^{*-}$  and  $B^- \rightarrow D^0\pi^-$ , as verified comparing generic Monte Carlo for  $B^- \rightarrow D^0K^{*-}$  and  $B^- \rightarrow D^0\pi^-$  data. For Sig we use a common  $m_{ES}$  resolution, while the mean value is taken different for  $B^- \rightarrow D^0K^{*-}$  and  $B^- \rightarrow D^0\pi^-$  in order to accomodate the apparent shift of  $\Delta m_{ES} = 1.7$  MeV/ $c^2$  for  $B^- \rightarrow D^0K^{*-}$  data. The MC values are used as starting point for the fit. The Argus end point is left floating and assumed to be the same for  $B^- \rightarrow D^0K^{*-}$  and  $B^- \rightarrow D^0\pi^-$  data. It was verified that the apparent  $m_{ES}$  shift for  $B^- \rightarrow D^0K^{*-}$  does not move the endpoint (this was checked by allowing two independent Argus endpoints, one for  $B^- \rightarrow D^0K^{*-}$  and one for  $B^- \rightarrow D^0\pi^-$ ). The  $\mathcal{F}$  discriminant is parameterized using two Gaussians, and the actual values of the parameters for Sig+ $B\bar{B}$  and Cont are taken common between  $B^- \rightarrow D^0K^{*-}$  and  $B^- \rightarrow D^0\pi^-$  data. Table 7 summarizes the values of the fixed parameters from MC, as well as the extracted from the yields and shapes fit (section 3.2).

<sup>7</sup>The interval  $\Delta E \in [-60, 100]$  MeV has been chosen in order to obtain a sufficiently large sideband while keeping outside peaking contributions from  $B$  decays with missing particles.

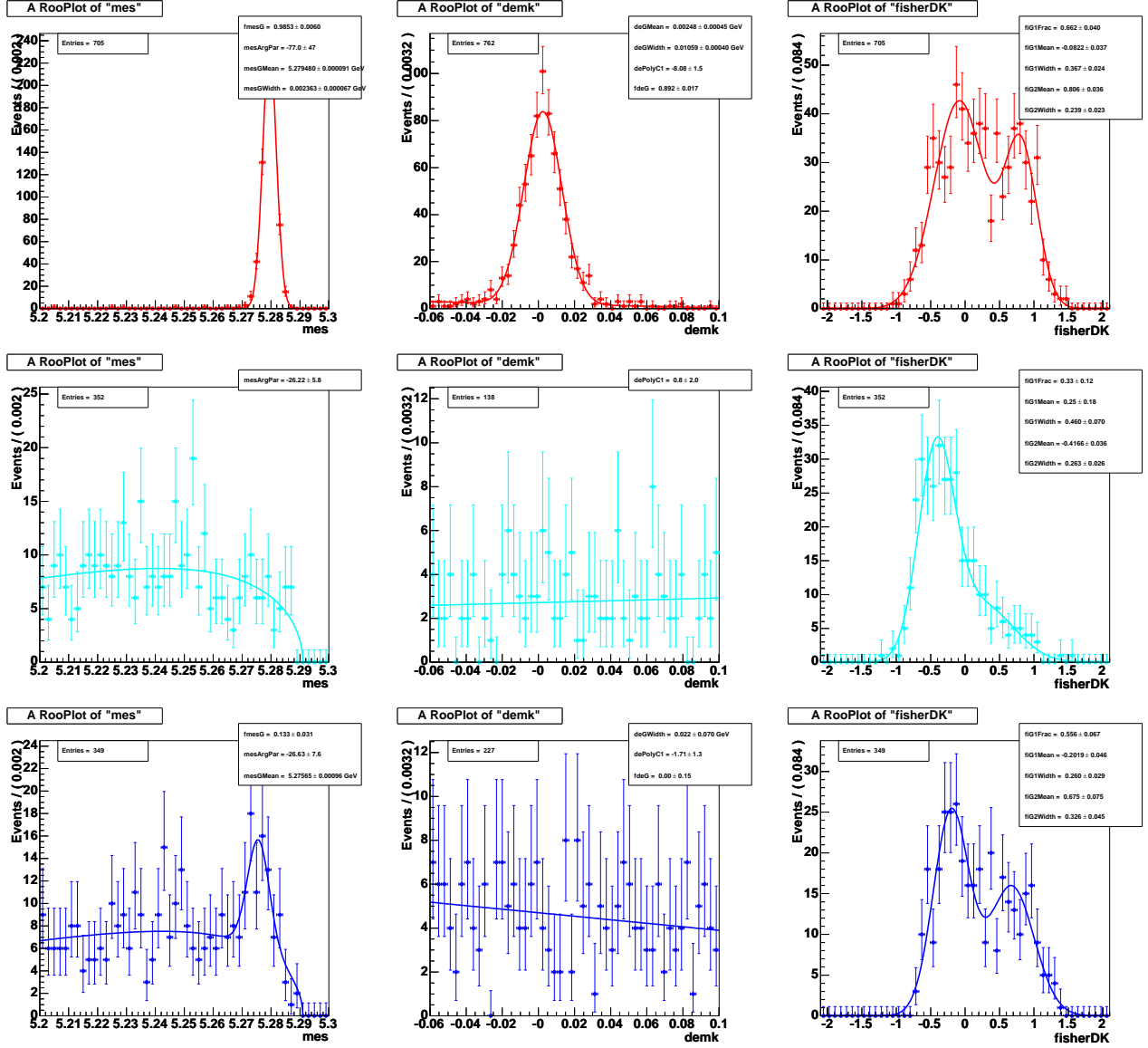


Figure 8:  $B^- \rightarrow D^0 K^{*-}$   $m_{ES}$  (left column),  $\Delta E$  (middle column) and  $\mathcal{F}$  (right column) shapes from Monte Carlo for Sig (top row), Cont (middle row), and  $B\bar{B}$  (bottom row). The  $\Delta E$  PDF shapes are shown only for reference since they are not used in the CP fit. Only the  $B\bar{B}$   $m_{ES}$  shape parameters are fixed to values found in Monte Carlo (as shown in Table 7). The Argus Cont and Gaussian Sig resolution parameters are extracted from the  $B^- \rightarrow D^0 \pi^-$  control sample, while the Gaussian mean value is determined from  $B^- \rightarrow D^0 K^{*-}$  data. The  $\mathcal{F}$  shapes in the final CP fit are extracted from the  $B^- \rightarrow D^0 \pi^-$  control sample (as given in Table 7), while the values indicated in this figure correspond to the Monte Carlo samples. The  $m_{ES}$  distributions are obtained for  $|\Delta E| < 25$  MeV, while the  $\mathcal{F}$  distributions are for  $|\Delta E| < 25$  and  $m_{ES} > 5.272$  GeV/ $c^2$ .

Shape parameter	
$m_{\text{ES}}$	
mesArgMax	$5.2893 \pm 0.0002$ GeV
mesContArgPar	$-23.7 \pm 3.8$
mesSigGMean	$5.2811 \pm 0.0004$ GeV
mesSigGWidth	$2.15 \pm 0.08$ MeV
mesBBCombArgPar	$-27 \pm 8$ (fixed from MC)
mesBBPkgGWidth	$0.0038 \pm 0.0014$ (fixed from MC)
fmesBBPkg	$0.133 \pm 0.031$ (fixed from MC)
$\mathcal{F}$	
fiContG1Frac	$0.55 \pm 0.05$
fiContG1Mean	$-0.463 \pm 0.014$
fiContG1Width	$0.220 \pm 0.014$
fiContG2Mean	$0.14 \pm 0.07$
fiContG2Width	$0.461 \pm 0.023$
fiSigG1Frac	$0.551 \pm 0.031$
fiSigG1Mean	$-0.176 \pm 0.026$
fiSigG1Width	$0.326 \pm 0.014$
fiSigG2Mean	$0.681 \pm 0.028$
fiSigG2Width	$0.311 \pm 0.015$

Table 7:  $B^- \rightarrow D^0 K^{*-}$  shape parameters as extracted from the  $m_{\text{ES}}$  and  $\mathcal{F}$   $B^- \rightarrow D^0 K^{*-}/B^- \rightarrow D^0 \pi^-$  combined fit. Only the  $B\bar{B}$   $m_{\text{ES}}$  shapes are taken from simulation.

### 3.1.2 Efficiency and Background Dalitz shapes

The Dalitz model PDF has to be corrected by efficiency non-uniformities across the Dalitz plot,  $\epsilon(m_+^2, m_-^2)$ . The correction has been obtained by performing an unbinned fit to a third order polynomial to the signal Monte Carlo where the  $D^0$  was allowed to decay isotropically (phase space),

$$P(x, y) = 1 + a_1 (x + y) + a_2 (x^2 + y^2 + xy) + a_3 (x^3 + y^3 + x^2y + xy^2). \quad (19)$$

The parameterization has been symmetrized for  $x = m_+^2$  and  $y = m_-^2$ . Figure 9 shows the Dalitz plot distribution and the  $m_+^2$  and  $m_-^2$  projections for this signal Monte Carlo sample. In this figure the blue curves represent the result of the 3rd order polynomial fit, and the red curves represent the projection for a perfectly flat efficiency. It can be seen that except at the borders of the kinematically allowed region the efficiency correction is quite consistent with a flat distribution. The resulting coefficients from the fit are given in Table 8.

The Dalitz distributions for the different background components,  $\mathcal{P}_j^{\text{comb}}$ ,  $j = \text{Cont}, B\bar{B}$ , have also to be estimated and used as input to the  $CP$  fit. They have been evaluated from continuum and generic  $B\bar{B}$  Monte Carlo events after having removed events with real  $D^0$ 's (using MC truth information). The selection cuts are identical to those used in the Dalitz  $CP$  fit. The distributions for  $q\bar{q}$  and  $B\bar{B}$  have been fitted (unbinned likelihood) to a symmetric second order polynomial function, as given in Eq. (19) with  $a_3 = 0$ . The distributions and fit results are shown in Figs. 10 and 11, for  $q\bar{q}$  and  $B\bar{B}$  respectively. The values of the parameters are given in Table 8. We have checked the parameterization by relaxing the  $\Delta E$  cut to  $[-60, 100]$  MeV, finding consistent values for the parameters, as shown in Table 8. The Cont Dalitz shape has also been extracted from

off-resonance data by selecting the  $D^0$  mass sidebands in order to exclude the real  $D^0$  (we required the  $D^0$  mass to be smaller than  $1.85 \text{ GeV}/c^2$  and larger than  $1.88 \text{ GeV}/c^2$ . Although the statistics is poor the shape from off-resonance data agrees with that observed from the  $q\bar{q}$  Monte Carlo.

Parameters	$a_1$	$a_2$	$a_3$
Efficiency ( $ \Delta E  < 25 \text{ MeV}$ )	$0.312 \pm 0.380$	$-0.087 \pm 0.152$	$0.008 \pm 0.023$
Cont( $ \Delta E  < 25 \text{ MeV}$ )	$-0.545 \pm 0.048$	$0.115 \pm 0.015$	0 (fixed)
$\text{B}\bar{\text{B}}$ ( $ \Delta E  < 25 \text{ MeV}$ )	$-0.649 \pm 0.020$	$0.1476 \pm 0.0085$	0 (fixed)
Cont( $\Delta E \in [-60, 100] \text{ MeV}$ )	$-0.583 \pm 0.033$	$0.148 \pm 0.011$	0 (fixed)
$\text{B}\bar{\text{B}}$ ( $\Delta E \in [-60, 100] \text{ MeV}$ )	$-0.617 \pm 0.016$	$0.1392 \pm 0.0063$	0 (fixed)

Table 8: *The values and the errors for the parameters of the third-order polynomial function, Eq. (19), obtained from the unbinned likelihood fit to the efficiency and Dalitz shape backgrounds for  $B^- \rightarrow D^0 K^{*-}$  events after symmetrization of the Dalitz plot ( $m_+^2$  vs  $m_-^2$ ), for  $|\Delta E| < 25 \text{ MeV}$  and  $m_{\text{ES}} > 5.2 \text{ GeV}/c^2$ .*

### 3.1.3 $D^0$ fractions

The fraction of true  $D^0$ 's ( $R$ ) and right-sign  $D^0$ 's  $R^{RS}$  for Cont and  $\text{B}\bar{\text{B}}$  events has been reevaluated on Monte Carlo events by counting as described in section 1 but now after applying the best candidate choice algorithm. The values are reported in Table 9, which are essentially unchanged compared to Table 6.

Fraction	Estimate from generic MC
$R_{\text{Cont}}$ (real $D^0$ 's in Cont)	$0.205 \pm 0.022$
$R_{\text{B}\bar{\text{B}}}$ (real $D^0$ 's in $\text{B}\bar{\text{B}}$ )	$0.180 \pm 0.021$
$R_{\text{Cont}}^{RS}$ ( $D^0 K^{*-}$ in Cont)	$0.53 \pm 0.06$
$R_{\text{B}\bar{\text{B}}}^{RS}$ ( $D^0 K^{*-}$ in $\text{B}\bar{\text{B}}$ )	$0.67 \pm 0.06$

Table 9:  *$B^- \rightarrow D^0 K^{*-}$   $D^0$  fractions as estimated from generic MC, for the region  $|\Delta E| < 25 \text{ MeV}$  and  $m_{\text{ES}} > 5.2 \text{ GeV}/c^2$ .*

### 3.1.4 Fraction of wrong sign signal ( $\kappa_{\text{SigWS}}$ )

According to the phase Monte Carlo ( $\text{Sig}_{ps}$ ) and applying the best candidate choice algorithm, the fraction  $\kappa_{\text{SigWS}}$  is found to be  $0.0043 \pm 0.0005$  for  $m_{\text{ES}} > 5.2 \text{ MeV}/c^2$ . Therefore this component has been neglected in the nominal fit.

## 3.2 Results from PDF shapes fit

Yields and PDF shapes were first extracted by performing a fit to the  $B^- \rightarrow D^0 K^{*-}$  data, following the strategy described above. Table 7 shows all shape parameters as extracted from this fit. The fit projections for  $m_{\text{ES}}$  and  $\mathcal{F}$  are shown in Fig. 12. The corresponding yields are given in table 10.

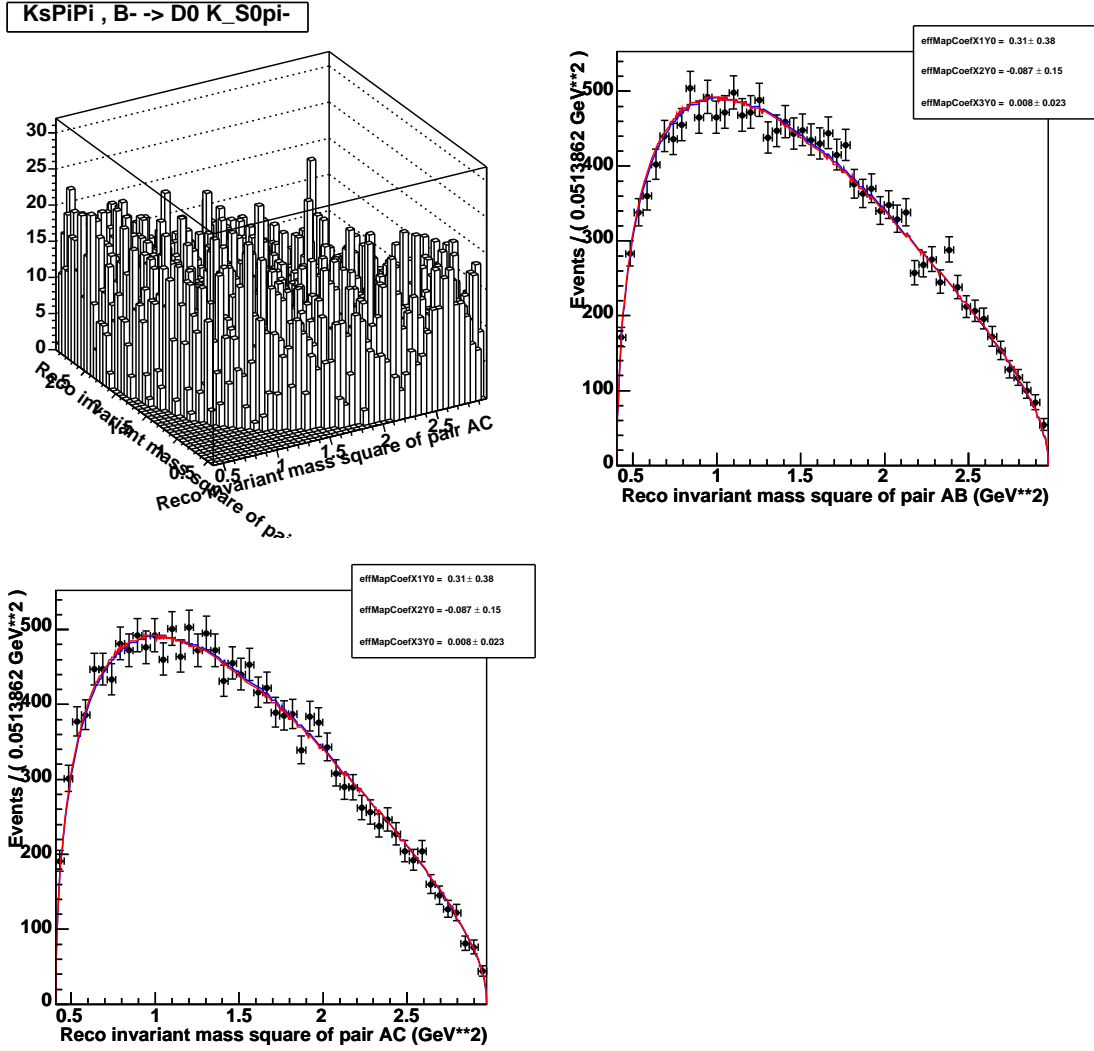


Figure 9:  $B^- \rightarrow D^0 K^{*-}$  Dalitz efficiency mapping for signal MC (phase space), for  $|\Delta E| < 25$  MeV and  $m_{ES} > 5.2$  GeV/ $c^2$  ( $m_{AB}^2 \equiv m_+^2$ ,  $m_{AC}^2 \equiv m_-^2$ ,  $m_{BC}^2 \equiv m_{\pi^+\pi^-}$ ). The blue curve is the result of an unbinned likelihood fit to a second order polynomial (after symmetrization of the Dalitz plot) to the  $B^- \rightarrow D^0 K^{*-}$  signal Monte Carlo, while the red curve corresponds to a phase space distribution.

Component	$D^0 K^*$ Yield
BB	$31 \pm 26$
Cont	$260 \pm 28$
Sig	$47 \pm 9$

Table 10:  $B^- \rightarrow D^0 K^{*-}$  yields from PDF shapes fit in  $\Delta E \in [-25, 25]$  MeV region.

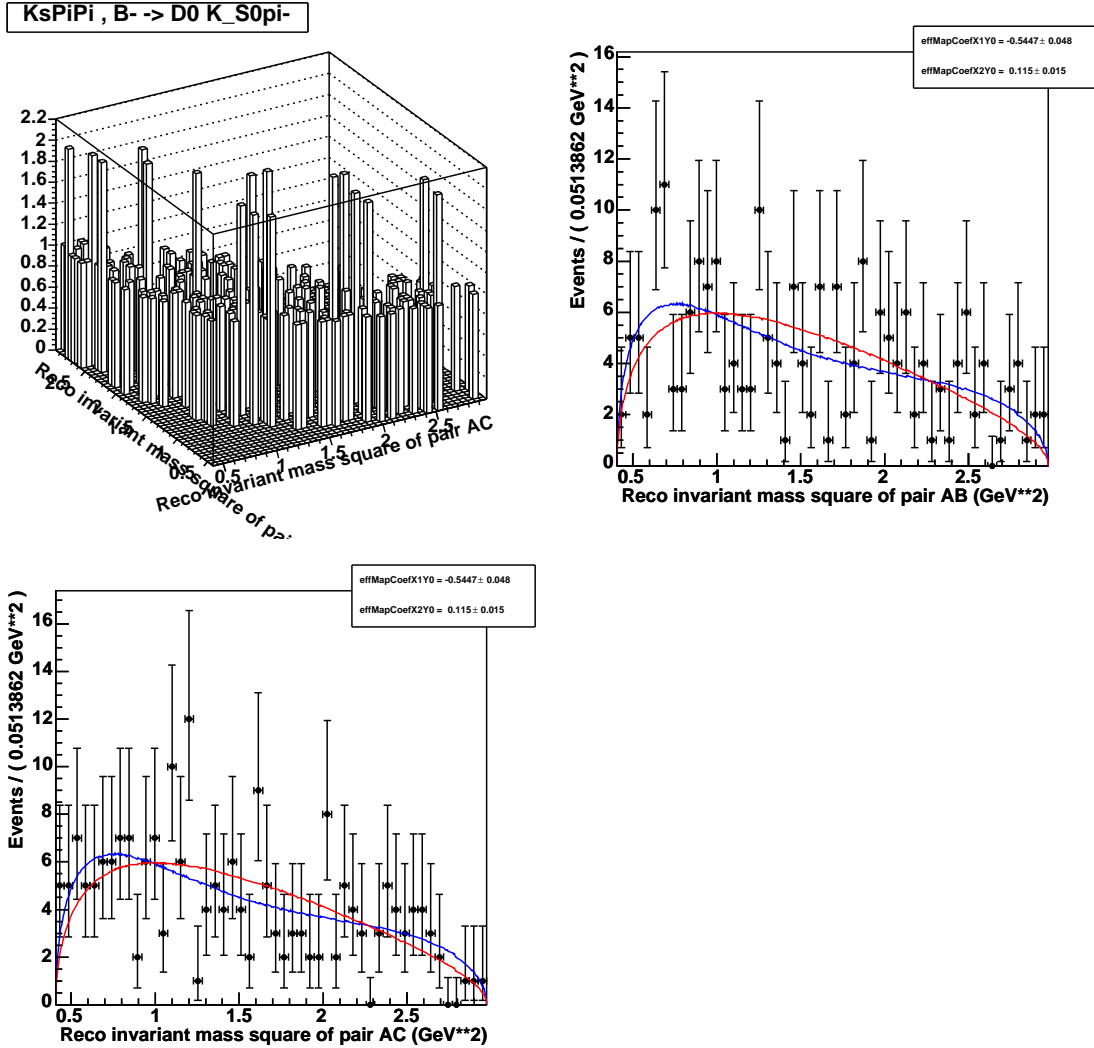


Figure 10:  $B^- \rightarrow D^0 K^{*0} \pi^-$  Cont background Dalitz shape from generic Monte Carlo, for  $|\Delta E| < 25$  MeV and  $m_{ES} > 5.2$  GeV/ $c^2$  ( $m_{AB}^2 \equiv m_+^2$ ,  $m_{AC}^2 \equiv m_-^2$  and  $m_{BC}^2 \equiv m_{\pi^+\pi^-}$ ). The blue curve is the result of an unbinned likelihood fit to a second order polynomial (after symmetrization of the Dalitz plot), while the red curve corresponds to a phase space distribution.

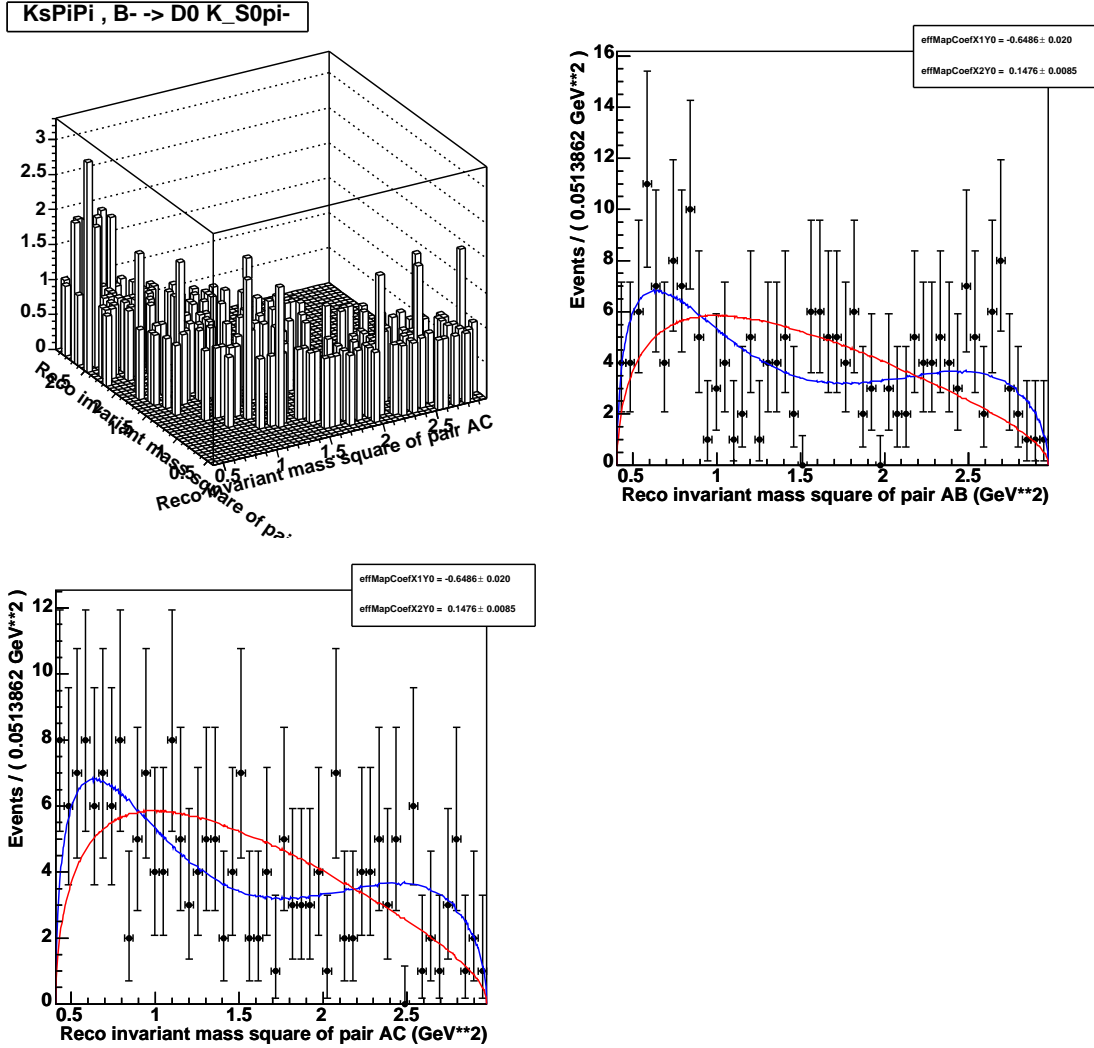


Figure 11:  $B^- \rightarrow D^0 K^{*-} \bar{B}\bar{B}$  background Dalitz shape from generic Monte Carlo, for  $|\Delta E| < 25$  MeV and  $m_{ES} > 5.2$  GeV/ $c^2$  ( $m_{AB}^2 \equiv m_+^2$ ,  $m_{AC}^2 \equiv m_-^2$  and  $m_{BC}^2 \equiv m_{\pi^+\pi^-}$ ). The blue curve is the result of an unbinned likelihood fit to a second order polynomial (after symmetrization of the Dalitz plot), while the red curve corresponds to a phase space distribution.

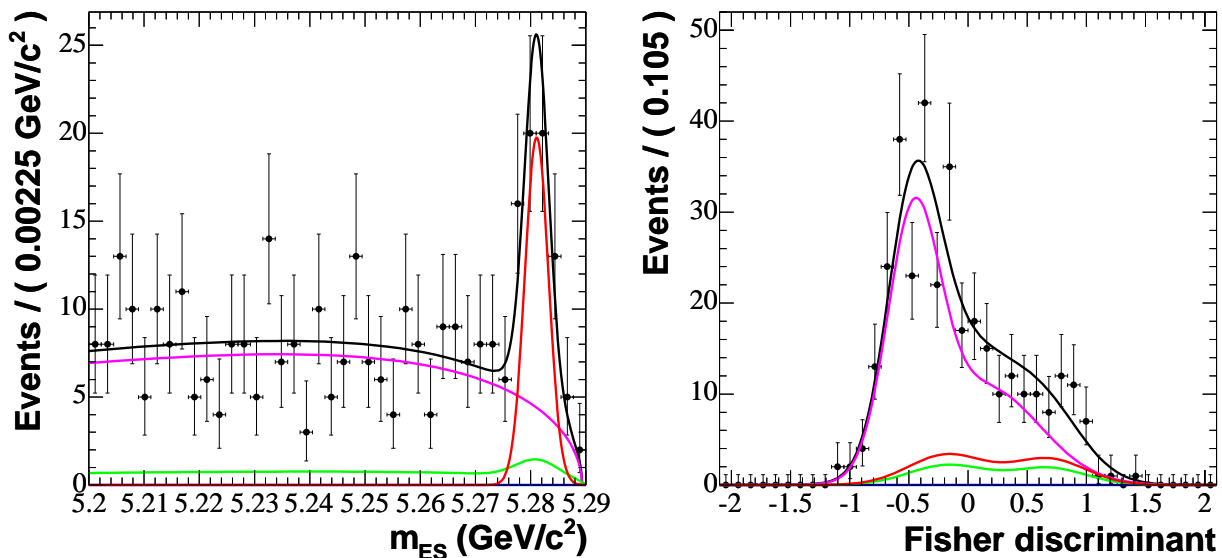


Figure 12:  $B^- \rightarrow D^0 K^{*-}$   $m_{ES}$ , and  $\mathcal{F}$  shapes extracted from the fit in the  $\Delta E$  region  $[-25, 25]$  MeV, compared to the data. Also shown are the different background components: Sig (red),  $B\bar{B}$  (green) and Cont (magenta).

### 3.3 Results from $CP$ fit

Table 11 reports the  $CP$  fit results for the cartesian  $x_{s\pm}$  and  $y_{s\pm}$  parameters, as defined in Eq. (14), with  $r_s^2$  floated as an independent parameter, for  $|\Delta E| < 25$  MeV. In this fit the PDF are fixed to the values found in the previous step, but the yields are refitted, together with the  $CP$  parameters. The correlation matrix between the five measurements are shown in Table 12. The obtained yields are given in Table 13. In Fig. 13 are shown the 39.3% and 86.5% confidence-level contours in the  $(x_{s\pm}, y_{s\pm})$  cartesian fit parameter space, corresponding to  $1\sigma$  and  $2\sigma$  two-dimensional ellipsoid regions respectively. The distance  $d$  is the length of the segment between the  $B^+$  (circle dot) and  $B^-$  (rectangular dot). The statistical significance of the  $CP$  violation will be discussed later in section 6. Given the good Gaussian behavior of the cartesian parameters, these contours have been obtained using the standard likelihood ratio method ( $\Delta \ln(\mathcal{L}_{exp}) = 1.0, 4.0$ , for 39.3% and 86.5% confidence-level regions). The fit projections for  $m_{ES}$  and  $\mathcal{F}$  are shown in Fig. 14. Finally, Figs. 15 and 16 show the Dalitz plot distributions for data and the fit projections, for the all Dalitz fit events ( $m_{ES} > 5.2$  GeV/ $c^2$ ) and for the signal box ( $m_{ES} > 5.272$  GeV/ $c^2$ ).

### 3.4 Nominal Toy Monte Carlo

The  $B^- \rightarrow D^0 K^{*-}$  Toy Monte Carlo samples were generated with parameters for  $m_{ES}$  and  $\mathcal{F}$  shapes and yields tuned to the data sample (Tables 7, 8, 9 and 13).

These samples are then fitted using the standard procedure (only  $CP$  part), using the nominal  $D^0 \rightarrow K_s^0 \pi^+ \pi^-$  Dalitz model. Figure 17 shows the residual, error and pull (defined as the residual divided by the error) distributions of the yields. The equivalent distributions for the cartesian  $CP$  parameters ( $x_{s-} \equiv reM$ ,  $y_{s-} \equiv imM$ ,  $x_{s+} \equiv reP$ ,  $y_{s+} \equiv imP$ ) are shown in Fig. 18. Figure 19 shows the equivalent distributions for  $r_s^2$ . For both the yields and the  $CP$  parameters (cartesian and

Observable	$D^0 K^*$
$x_{s-}$	$-0.197^{+0.205}_{-0.204} [\pm 0.201]$
$y_{s-}$	$+0.255^{+0.300}_{-0.303} [\pm 0.303]$
$x_{s+}$	$-0.066^{+0.229}_{-0.241} [\pm 0.234]$
$y_{s+}$	$-0.011^{+0.349}_{-0.308} [\pm 0.324]$
$r_s^2$	$0.051^{+0.144}_{-0.093} [\pm 0.114]$

Table 11: *Fit results on data for  $(x_{s\pm}, y_{s\pm})$  cartesian coordinates for the  $B^- \rightarrow D^0 K^{*-}$  decay mode. The values inside brackets are the quadratic (Gaussian) errors calculated from the fit covariance matrix.*

Observable	$x_{s-}$	$y_{s-}$	$x_{s+}$	$y_{s+}$	$r_s^2$
$x_{s-}$	1	$1.00 \times 10^{-1}$	$8.21 \times 10^{-2}$	$-4.05 \times 10^{-2}$	$-2.26 \times 10^{-1}$
$y_{s-}$		1	$-2.0 \times 10^{-2}$	$5.15 \times 10^{-3}$	$3.71 \times 10^{-2}$
$x_{s+}$			1	$2.16 \times 10^{-2}$	$-2.51 \times 10^{-1}$
$y_{s+}$				1	$2.20 \times 10^{-1}$
$r_s^2$					1

Table 12: *Correlation matrix for  $(x_{s\pm}, y_{s\pm})$  cartesian coordinates, for the  $B^- \rightarrow D^0 K^{*-}$  decay mode.*

Component	$D^0 K^*$ Yield
BB	$45 \pm 21$
Cont	$251 \pm 24$
Sig	$42 \pm 8$

Table 13:  *$B^- \rightarrow D^0 K^{*-}$  yields from the CP fit.*

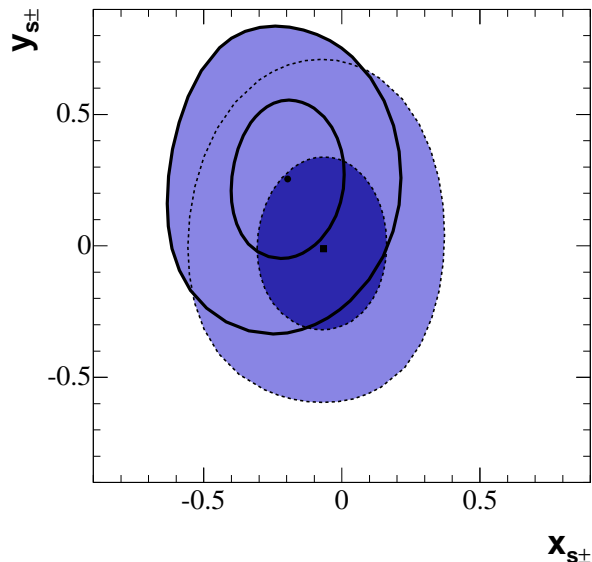


Figure 13: 39.3% (dark blue) and 86.5% (bright blue) confidence-level contours, corresponding to  $1\sigma$  and  $2\sigma$  two-dimensional ellipsoid regions, in the  $(x_{s\pm}, y_{s\pm})$  cartesian fit parameter space for  $B^- \rightarrow D^0 K^{*-}$ . Solid (dotted) contours are for  $B^-$  ( $B^+$ ) decays. Given the good Gaussian behavior of the cartesian parameters, these contours have been obtained using the standard likelihood ratio method,  $\Delta \ln(\mathcal{L}_{exp}) = 1.0, 4.0$ .

$r_s^2$ ) the fit behaves well: no significant biases are observed and the Gaussian behavior is satisfied. There is good agreement between the fit errors on data (red arrows) and those predicted by the MC experiments. The distribution of log-likelihood values for the nominal Toy MC is shown in figure 20. The arrow indicates the value found on the data sample, which provides a good goodness-of-fit (about 50%).

In order to check whether floating  $r_s^2$  increases the statistical error on the cartesian coordinates, a similar Toy Monte Carlo study was performed using a configuration where  $r_s^2$  was generated and fitted with a fixed value of 0.04, corresponding to a  $r_s \approx 0.2$ . The usual residual, error and pull distributions for the cartesian  $CP$  parameters, shown in Figure 21, reveal that the statistical sensitivity is essential unchanged with  $r_s^2$  either fixed or floated.

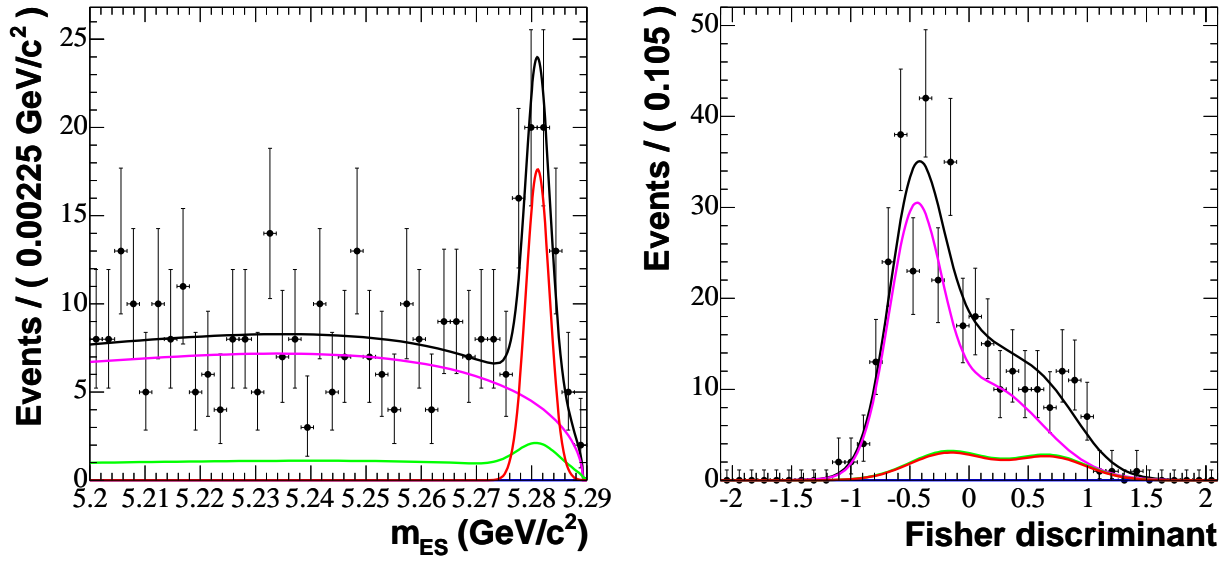


Figure 14:  $B^- \rightarrow D^0 K^{*-}$   $m_{ES}$  and  $\mathcal{F}$  shapes from the Dalitz CP fit compared to the data. The shapes are fixed to the values found from the shapes prefit while the Sig, Cont and  $B\bar{B}$  yields are refloated exploiting the Dalitz plot as additional discriminant variable. Also shown are the different background components: Sig (red),  $B\bar{B}$  (green) and Cont (magenta).

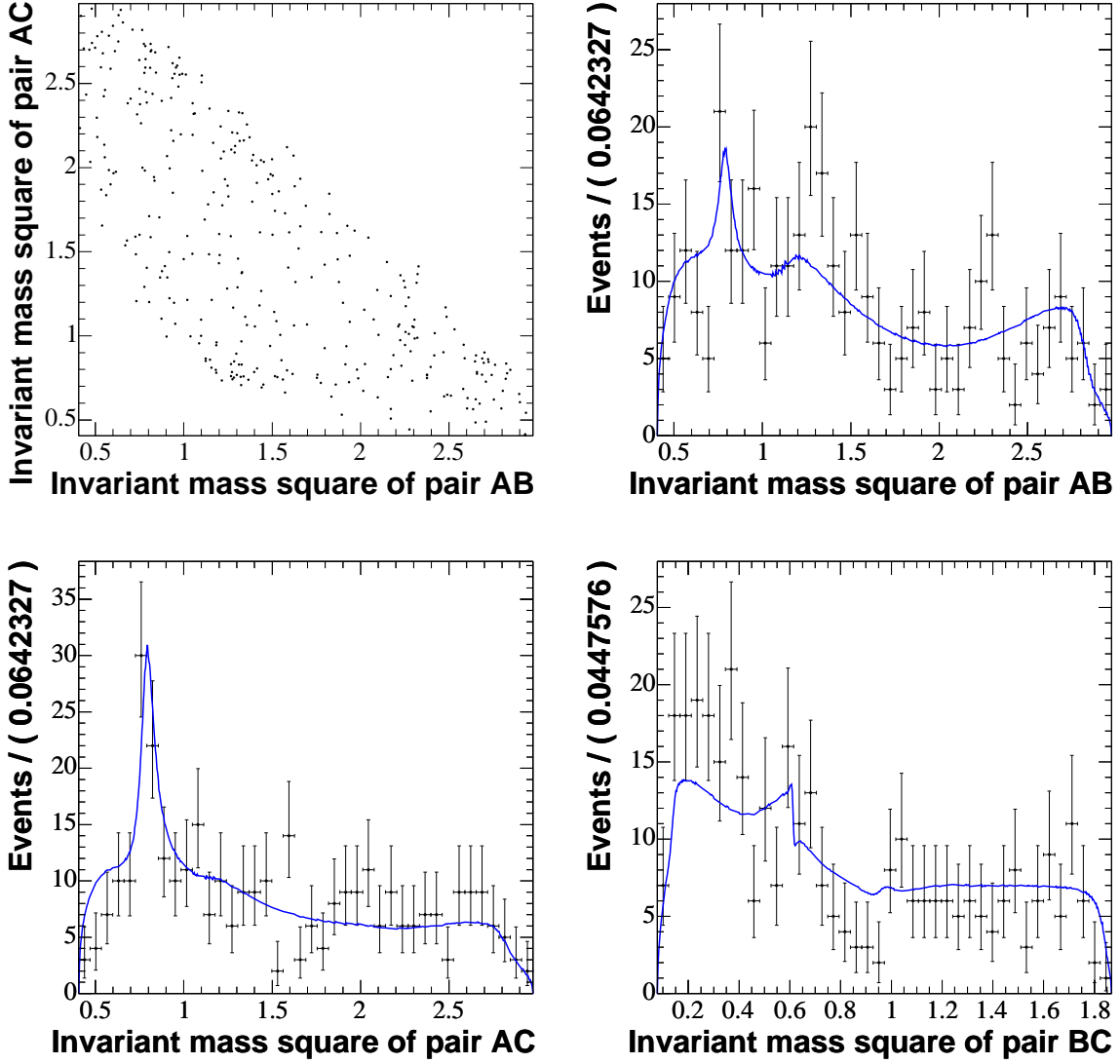


Figure 15:  $B^- \rightarrow D^0 K^{*-}$  Dalitz plot and their projections from the CP fit for events with  $|\Delta E| < 25$  MeV and  $m_{ES} > 5.2$  GeV/c<sup>2</sup> ( $m_{AB}^2 \equiv m_+^2$ ,  $m_{AC}^2 \equiv m_-^2$ ,  $m_{BC}^2 \equiv m_{\pi^+\pi^-}$ ).

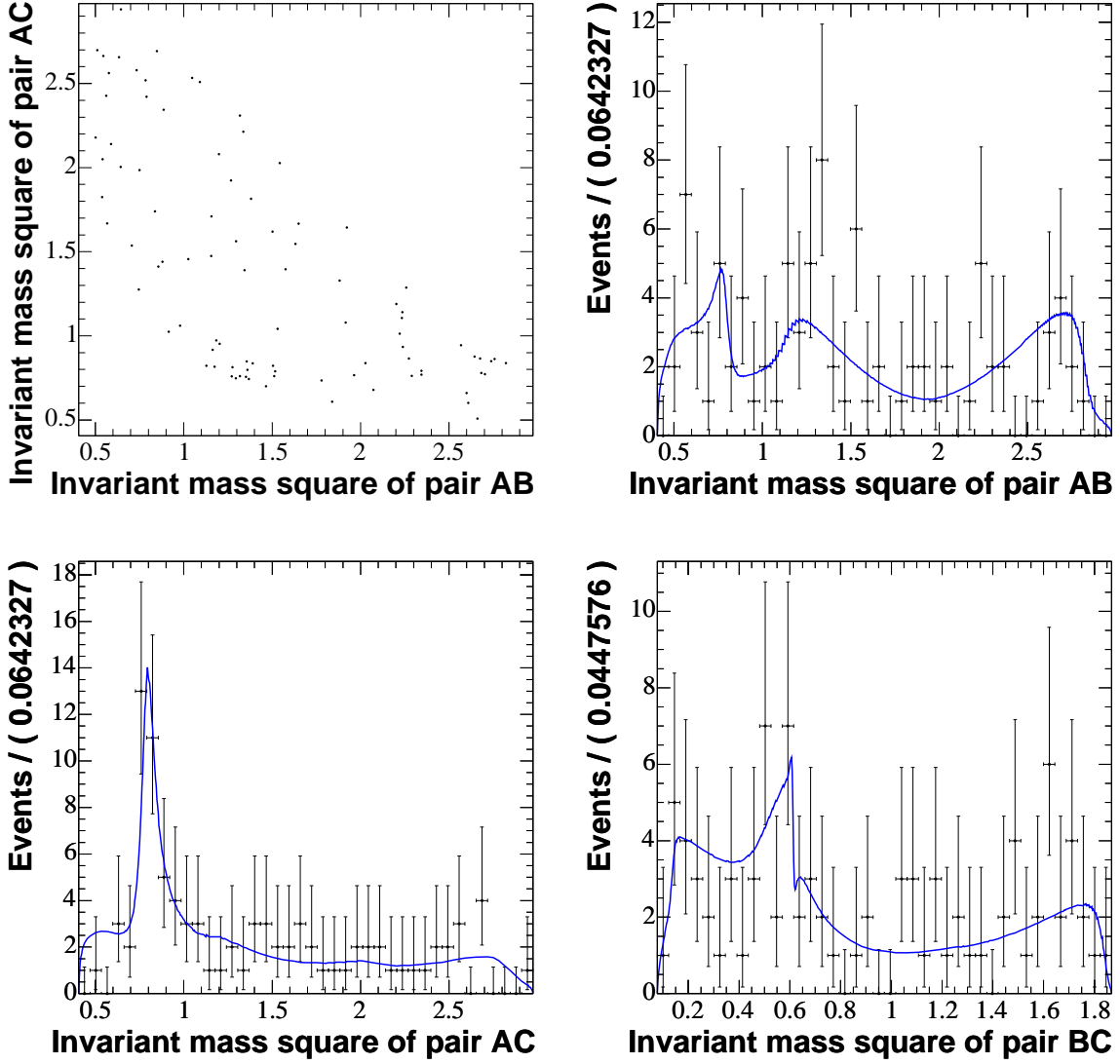
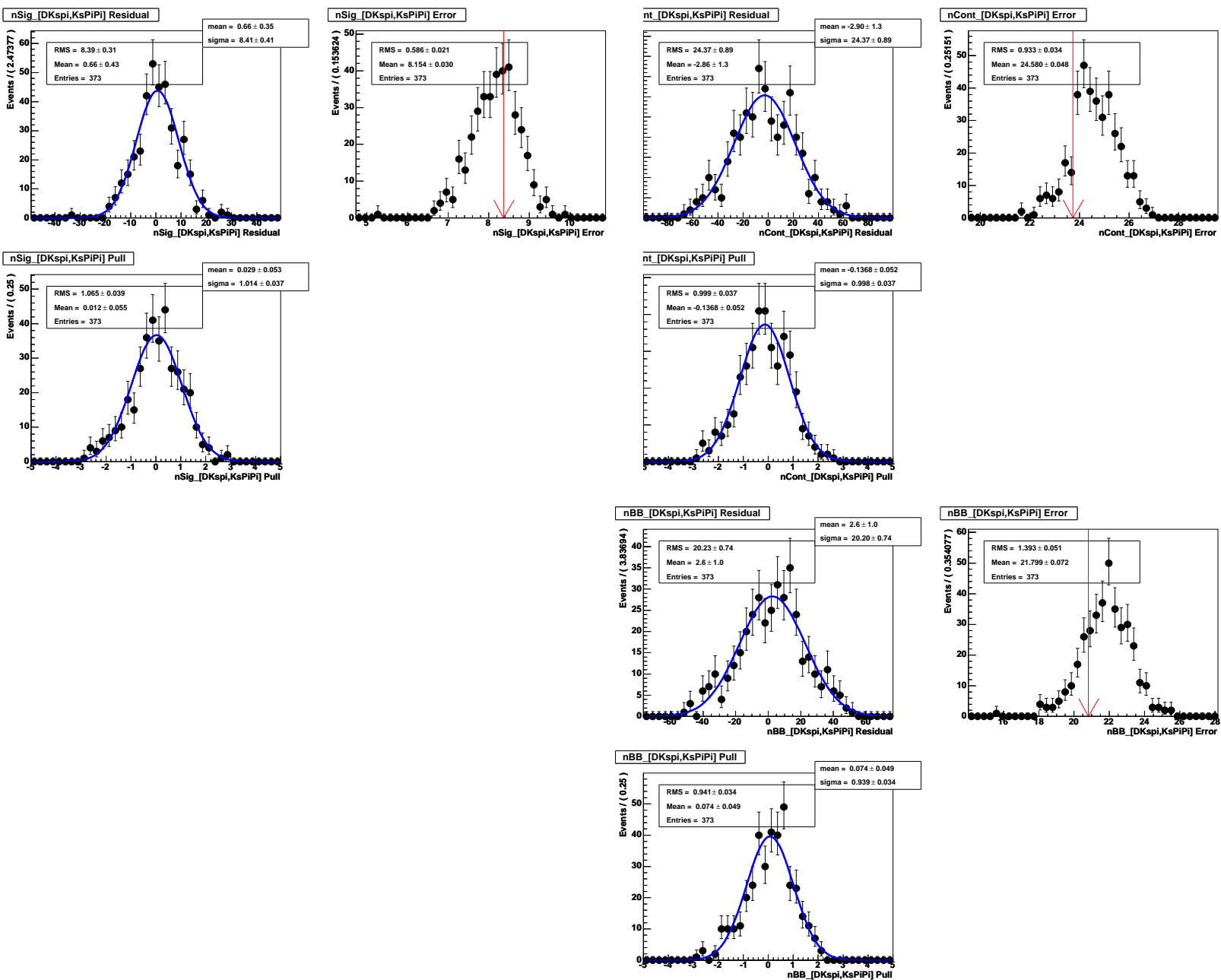


Figure 16:  $B^- \rightarrow D^0 K^{*-}$  Dalitz plot and their projections from the CP fit for events with  $|\Delta E| < 25$  MeV and  $m_{ES} > 5.272$  GeV/ $c^2$  ( $m_{AB}^2 \equiv m_+^2$ ,  $m_{AC}^2 \equiv m_-^2$ ,  $m_{BC}^2 \equiv m_{\pi^+\pi^-}$ ).

Figure 17: Residual, error and pull distributions for the BB (top left in landscape), Cont (top right in landscape) and Sig (bottom in landscape) components for the  $B^- \rightarrow D^0 K^{*-}$  sample from the nominal Toy MC.



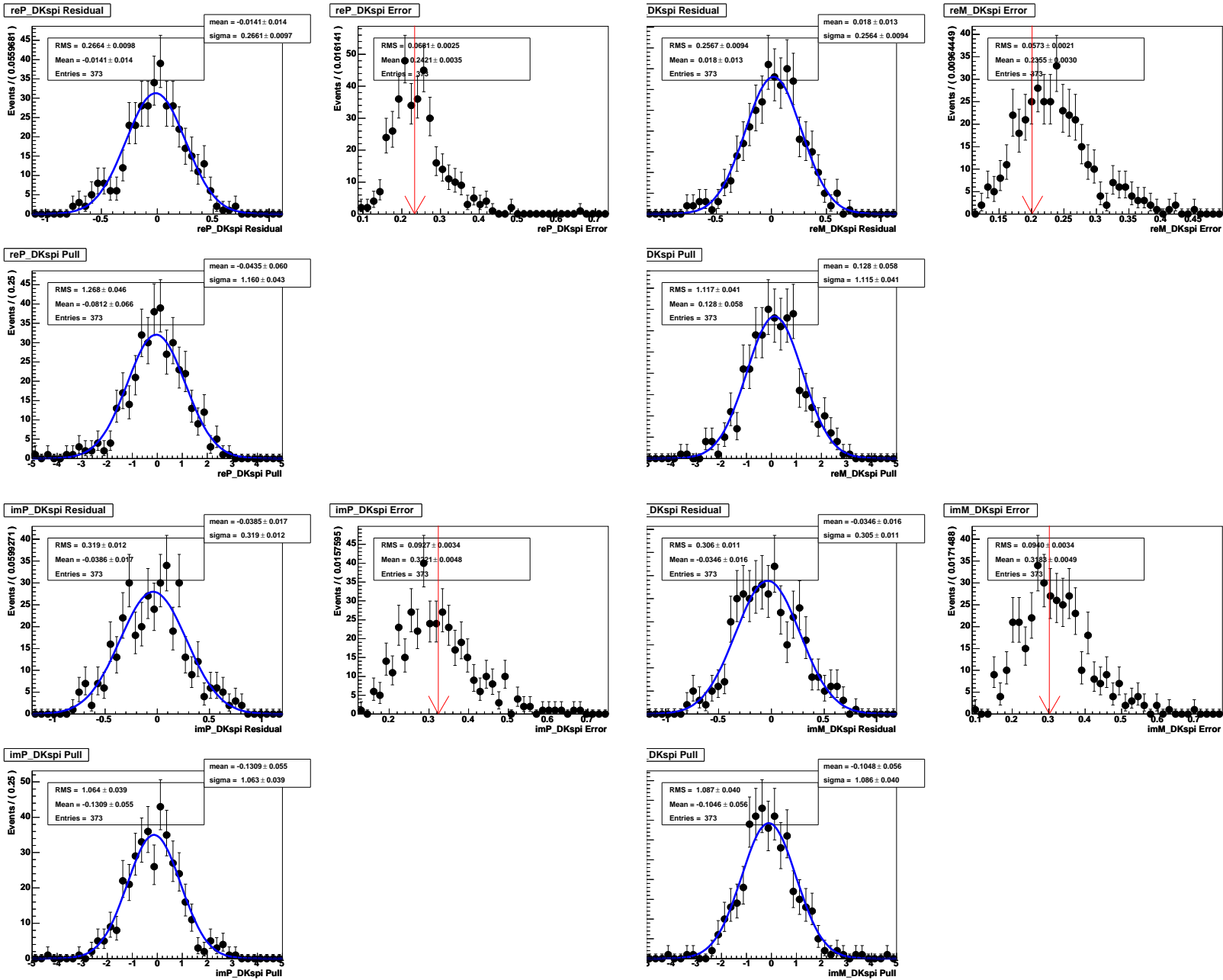


Figure 18: Residual, error and pull distributions for  $x_{s+} \equiv reP$  (top left in landscape),  $x_{s-} \equiv reM$  (top right in landscape),  $y_{s+} \equiv imP$  (bottom left in landscape), and  $y_{s-} \equiv imM$  (top right in landscape), for the  $B^- \rightarrow D^0 K^{*-}$  sample for the nominal Toy MC.

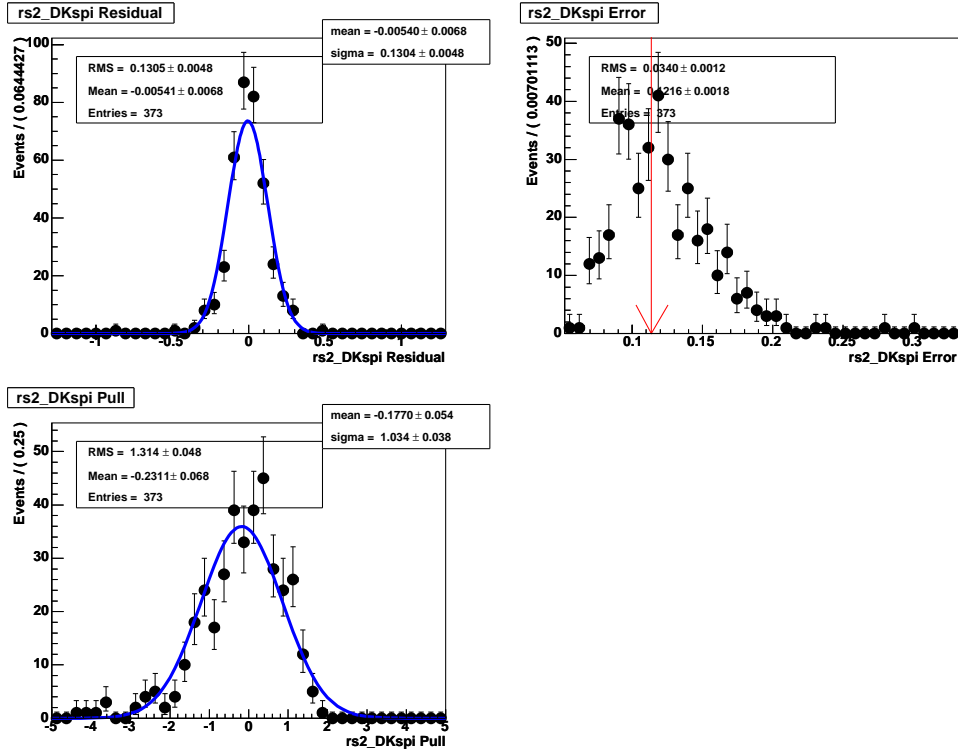


Figure 19: Residual, error and pull distributions for  $r_s^2$  for the  $B^- \rightarrow D^0 K^{*-}$  sample for the nominal Toy MC.

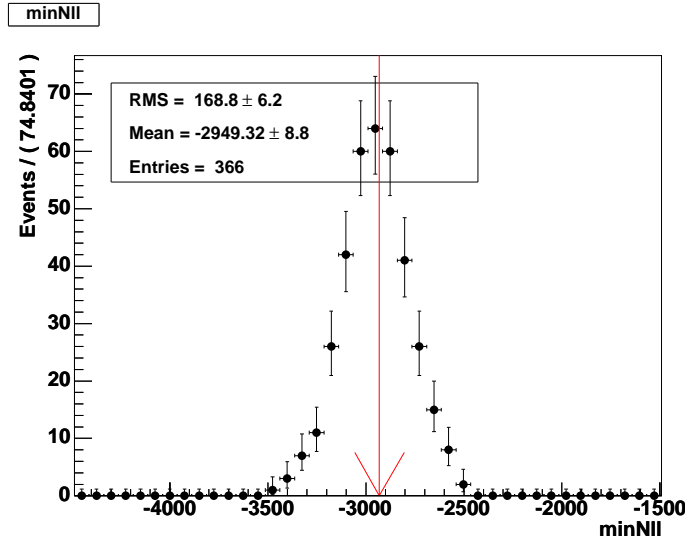


Figure 20: Distribution of log-likelihood values for the nominal toy MC. The arrow indicates the value obtained in the data set fit. The agreement with expectations is remarkable, providing a goodness-of-fit of about 50%.

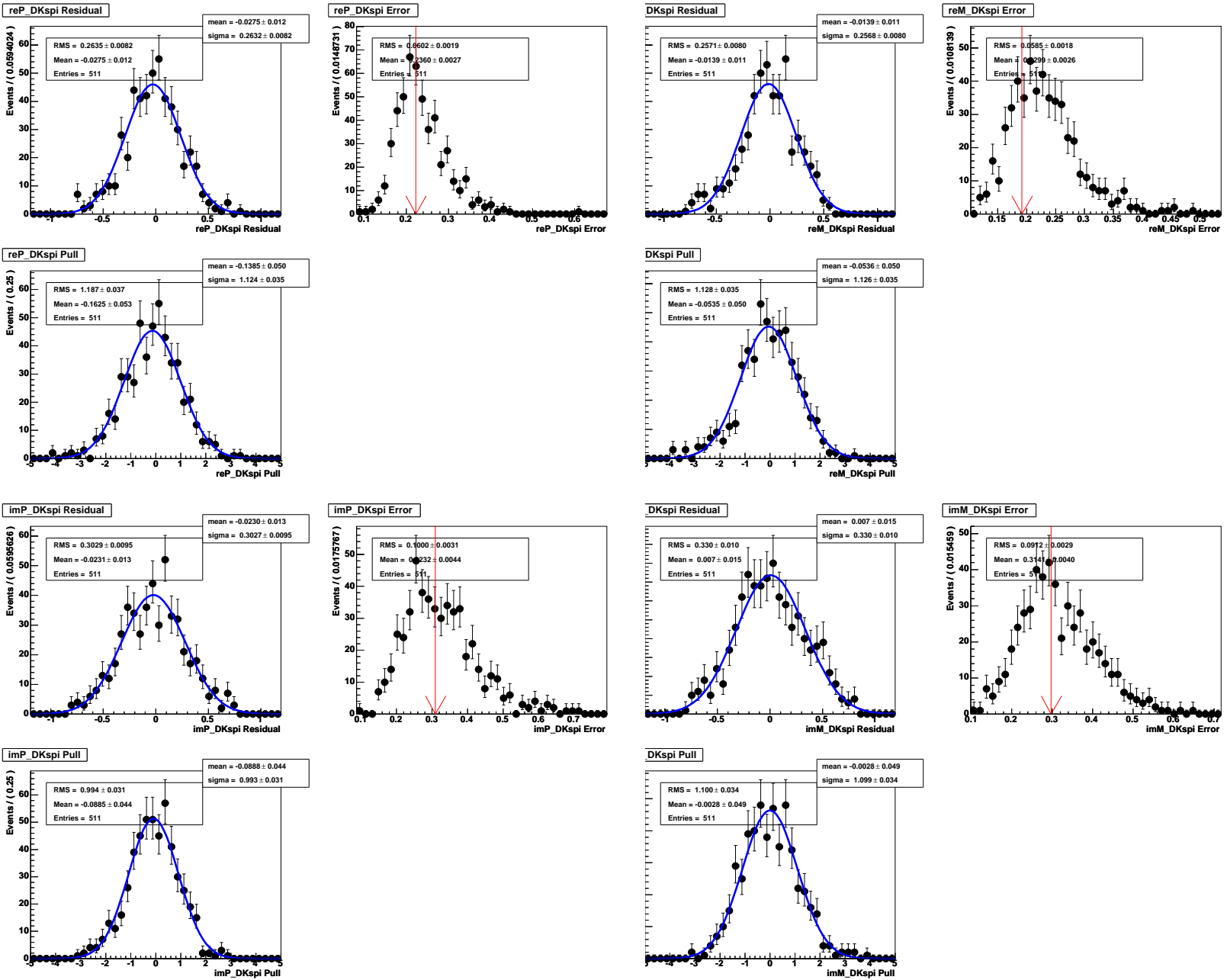


Figure 21: Residual, error and pull distributions for  $x_{s+} \equiv reP$  (top left in landscape),  $x_{s-} \equiv reM$  (top right in landscape),  $y_{s+} \equiv imP$  (bottom left in landscape), and  $y_{s-} \equiv imM$  (top right in landscape), for the  $B^- \rightarrow D^0 K^{*-}$  sample for a Toy MC tuned to the data with  $r_s^2$  fixed to 0.04.

## 4 Experimental systematic uncertainties

Table 15 summarizes the main systematic uncertainties of the measurement in cartesian coordinates, for the  $B^- \rightarrow D^0 K^{*-}$  decay mode. For comparison, we indicate the Dalitz model systematics by using the K-matrix model and the CLEO model (old method).

Source	$x_{s+}$	$y_{s+}$	$x_{s-}$	$y_{s-}$
$m_{\text{ES}}, \mathcal{F}$ shapes	0.098	0.116	0.079	0.116
Real $D^0$ fraction	0.028	0.036	0.033	0.025
Right sign $D^0$ 's	0.033	0.047	0.032	0.042
Efficiency in the Dalitz plot	0.067	0.091	0.059	0.044
Tracking efficiency	0.008	0.011	0.010	0.012
Background Dalitz shape	0.038	0.091	0.044	0.087
Invariant mass resolution	0.003	0.002	0.002	0.002
Dalitz amplitude and phases	0.004	0.014	0.008	0.008
SubTotal	0.132	0.184	0.118	0.160
Dalitz model (K-matrix)	0.007	0.006	0.008	0.006
Dalitz model (CLEO model)	0.033	0.046	0.034	0.034
Total (CLEO model)	0.136	0.190	0.123	0.163

Table 14: *Summary of the contributions to the systematic error in cartesian coordinates ( $x_{s\pm}, y_{s\pm}$ ).*

In the following subsections we describe how each systematic uncertainty contribution in the cartesian coordinate space has been evaluated.

### 4.1 $m_{\text{ES}}$ and Fisher shapes

The effect of fixing the PDF shapes in the  $CP$  fit has been evaluated by performing a simultaneous PDF shape and  $CP$  fit. The  $CP$  and shapes fit is performed simultaneously to the  $B^- \rightarrow D^0 K^{*-}$  and  $D\pi$  samples, with shapes fixed and floated. The systematics was then taken as the quadratic difference of the errors reported by the two fits. The  $m_{\text{ES}}$  endpoint in the Argus parameterization is left floating in the nominal fit. In the estimate of the systematic error we have also evaluated the effect of the fraction of peaking  $B\bar{B}$  background, which is fixed in the nominal fit. We have varied that fraction within the error calculated on signal Monte Carlo. Similarly we have evaluated the effect of fixing the shape (from Monte Carlo estimate) of the  $B\bar{B}$  Argus parameterization for  $m_{\text{ES}}$ . In all cases the difference between the central values of the two fits is well below the statistical difference.

### 4.2 Background composition

The fraction of real  $D^0$  has been estimated from data and Monte Carlo as explained in Section. 1.3, the two values agree within the error. The uncertainty due to the fraction of real  $D^0$ 's in background (table 9) is estimated by varying this parameter within its statistical error from the  $D^0$  mass fit on data, and then repeating the fit to the data sample. The larger between the half difference between the two fits and the quadratic difference of the fit errors is assigned as systematic uncertainty.

A potential difference in the number of real  $D^0$ 's in the continuum background between  $B^+$  and  $B^-$  events could fake  $CP$  violating effects in the signal. No significant difference between  $B^+$  and  $B^-$  has been found in MC. Nevertheless, we account for any potential effect by introducing an

independent set of  $CP$  parameters for the continuum background with a real  $D^0$ . By repeating the nominal fit with this new set of parameters we found a negligible impact on the  $CP$  parameters.

The fraction of right sign (RS)  $D^0$ 's is taken from MC simulation. We have estimated this contribution from the variation of the  $CP$  parameters in the fit to the data sample when a value of 0.5 is assumed instead of the nominal values (given in table 9). As before, we take the larger between the difference of central values and the quadratic difference of fit errors. The change observed on the  $CP$  parameters is consistent with the larger between the bias and the rms from a set of Toy MC experiments generated with the nominal value and fit with 0.5.

### 4.3 Dalitz efficiency

To estimate the effect from the Dalitz efficiency the nominal  $CP$  fit was repeated by assuming a flat distribution instead of the nominal 3rd order polynomial parameterization (table 8). In addition, we have evaluated a systematic due to tracking and  $K_s^0$  reconstruction efficiency over the Dalitz plot. It has been evaluated by repeating the fit using alternative values of the 3rd order polynomial parameterization coefficients with: i) the tracking efficiency correction applied on the 2 pions from the  $D^0$  decay and the bachelor kaon (table 10 of Ref. [4]); and ii) tracking efficiency correction applied to the pions from the  $K_s^0$  decay (table 11 of Ref. [4]). In all cases, we take the larger between the difference of central values and the quadratic difference of fit errors. The uncertainties from the two corrections have been added quadratically.

### 4.4 Dalitz shape for combinatorial background

The correction for Cont and  $B\bar{B}$  combinatorial background is obtained from Monte Carlo simulation. The systematic from this correction is estimated from the difference on the  $CP$  parameters when flat distributions are assumed instead. We take the larger between the difference of central values and the quadratic difference of fit errors. As further check we have varied the parameterization for the combinatorial background using a third order (most general) two-dimensional symmetric polynomial function and a second order (most general) two-dimensional polynomial function. The effect due to the alternative parameterizations was compatible with the systematic error we have quoted.

### 4.5 Limited mass resolution

The nominal Dalitz model assumes perfect mass resolution. Given that all the resonances present in the  $D^0 \rightarrow K_s^0 \pi^+ \pi^-$  decay are quite wide compared to the estimated mass resolution (about 4 MeV<sup>2</sup> for a  $K_s^0 \pi^+$  mass squared of about 1 GeV<sup>2</sup> [13]), we expect the effect to be completely negligible. Only the  $\omega(782)$  has an intrinsic width comparable to the mass resolution (about 6 MeV<sup>2</sup> for a squared  $\pi^+ \pi^-$  mass of 0.8 GeV<sup>2</sup> [13]), but the sensitivity of the  $CP$  parameters is in this case suppressed. To evaluate the effect of the limited mass resolution on the Dalitz plot, two different fits were performed to the reweighted signal MC (see section 10.3 of Ref. [4]). The first fit used the reconstructed  $K_s^0 \pi^+$  and  $K_s^0 \pi^-$  masses, while the second was performed with the MC truth masses (perfect resolution). The difference of fit values was taken as our systematic uncertainty. The errors from the fit for the different parameters were basically unchanged between the two fits.

## 4.6 Statistical errors on Dalitz amplitudes and phases

The phases and amplitudes of the Dalitz model are fixed to the values found from the fit to the high statistics  $D^{*+} \rightarrow D^0 \pi_s^+$  sample. We expect that the effect coming from the statistical errors on the Dalitz amplitudes and phases is not large. We estimated its effect in the  $B^- \rightarrow D^0 K^-$  analysis by performing a simultaneous  $DK$  and  $D^{*+} \rightarrow D^0 \pi_s^+$  fit with all these parameters floated, as documented in [12] (table 11 and sec. 3.7). The uncertainty was taken as the largest value between the difference of central values and the quadratic difference of the errors reported by the two fits. The difference of central values is in all cases consistent with the quadratic difference of the statistical errors.

## 4.7 Wrong sign signal fraction

Due to the very small value of  $\kappa_{\text{sigWS}}$  found in the Monte Carlo simulation,  $0.0043 \pm 0.0005$ , this effect is completely negligible.

## 5 Dalitz model systematic uncertainty

The systematic uncertainty related to the phenomenological parameterization of the  $D^0$  decay amplitude represents the main systematic error of the analysis. In the ICHEP analysis, we estimated this effect using alternative amplitude parameterizations, as the CLEO model [4, 12] and the model without the  $\sigma_1$ ,  $\sigma_2$  scalar ( $\pi^+\pi^-$ ) resonances. Variations of the parameters for the Breit-Wigner functions, for the vertex factors and of the Blatt-Weisskopf factors gave smaller effects. Although  $\sigma_1$  and  $\sigma_2$  are not established resonances, we introduced them in the Dalitz parameterization to better fit the data distribution. In this updated analysis, we have used the K-matrix technique to parametrize the ( $\pi^+\pi^-$ ) S-wave contribution, as documented in BAD1237. It is a more appropriate technique to parametrize the scalar ( $\pi^+\pi^-$ ) S-wave amplitude, which removes the explicit dependence on (not-established) scalar resonances. Conservatively we have decided to quote both the errors obtained with the CLEO and the K-Matrix alternative models, reported in Tables 15, 16 for the  $B^- \rightarrow D^0 K^{*-}$  decay mode. The exp-by-exp distributions are shown in Figures 22, 23, 24, 25.

Source	$x_{s+}$	$y_{s+}$	$x_{s-}$	$y_{s-}$
Dalitz model (CLEO)	0.0326	0.0460	0.0340	0.0335
Dalitz model (K-Matrix)	0.0073	0.0065	0.0083	0.0060

Table 15: *Systematic errors, due to the  $D^0$  amplitude model, on the cartesian coordinates,  $(x_{s\pm}, y_{s\pm})$  for the  $B^- \rightarrow D^0 K^{*-}$  decay mode.*

Source	$kr_s$	$\gamma$ (deg.)	$\delta_s$ (deg.)
Dalitz model (CLEO)	0.0452	8.9	11.0
Dalitz model (K-Matrix)	0.0152	3.2	2.2

Table 16: *Systematic errors, due to the  $D^0$  amplitude model, on the physics parameters,  $kr_s$ ,  $\gamma$ ,  $\delta_s$  for the  $B^- \rightarrow D^0 K^{*-}$  decay mode.*

For completeness we report also the estimates of systematic error due to the  $D^0$  amplitude parameterization for the  $B^- \rightarrow D^{(*)0} K^-$  decay modes in Tables 17, 18. The exp-by-exp distributions are shown in Figures 26, 27, 28, 29.

Source	$x_+$	$y_+$	$x_-$	$y_-$	$x_+^*$	$y_+^*$	$x_-^*$	$y_-^*$
Dalitz model (CLEO)	0.0317	0.053	0.0187	0.0215	0.0251	0.0676	0.0222	0.0270
Dalitz model (K-Matrix)	0.005	0.007	0.0025	0.0033	0.0031	0.0045	0.0068	0.0061

Table 17: *Systematic errors, due to the  $D^0$  amplitude model, on the cartesian coordinates  $(x_{\pm}, y_{\pm}, x_{\pm}^*, y_{\pm}^*)$  for the  $B^- \rightarrow D^{(*)0} K^-$  decay mode.*

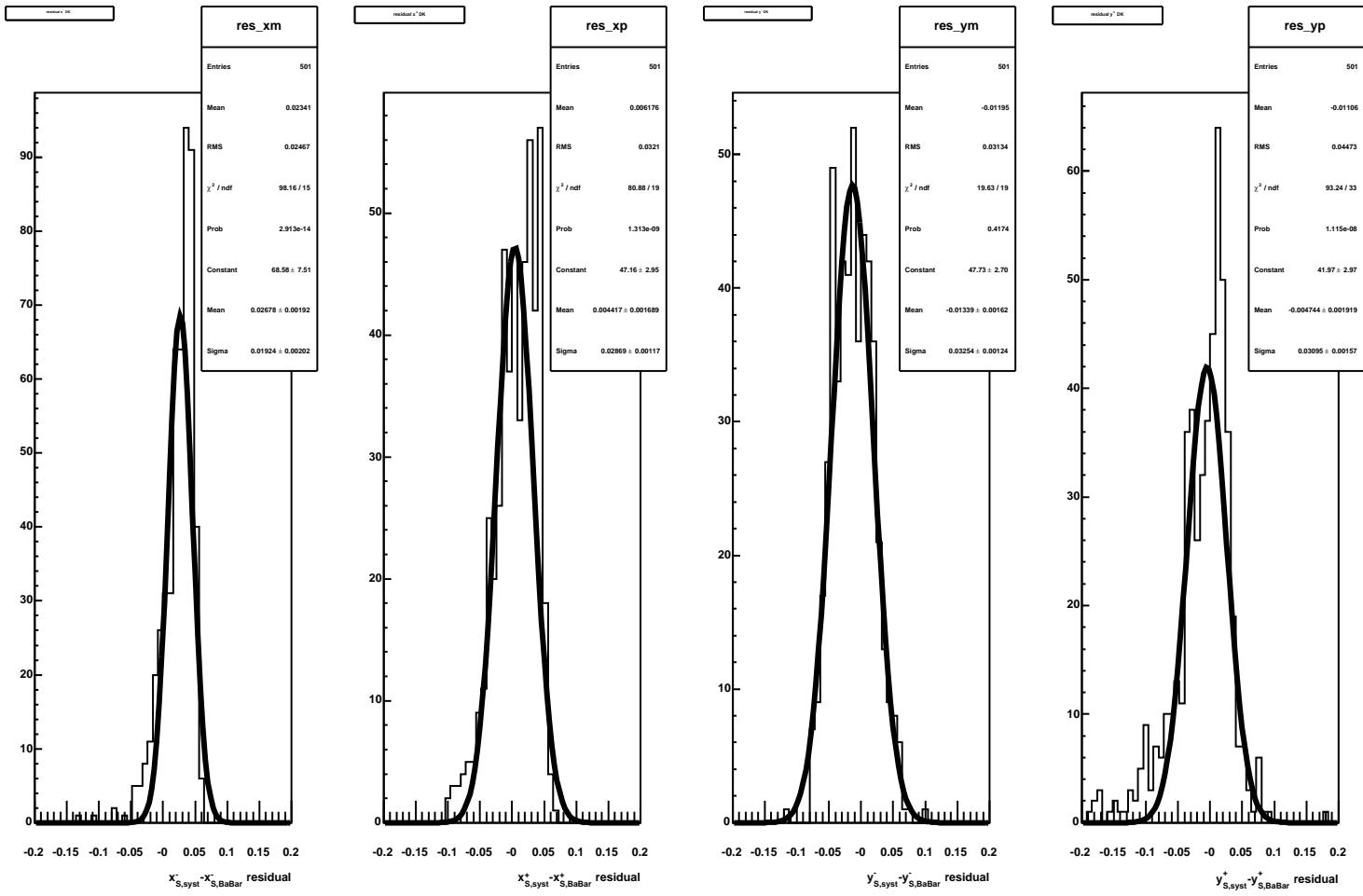


Figure 22: Experiment-by-experiment differences of the cartesian CP fit parameters using the reference and the CLEO Dalitz models for the  $B^- \rightarrow D^0 K^{*-}$  decay mode. The systematic error for each component is quoted as quadratic sum of the bias and the rms.

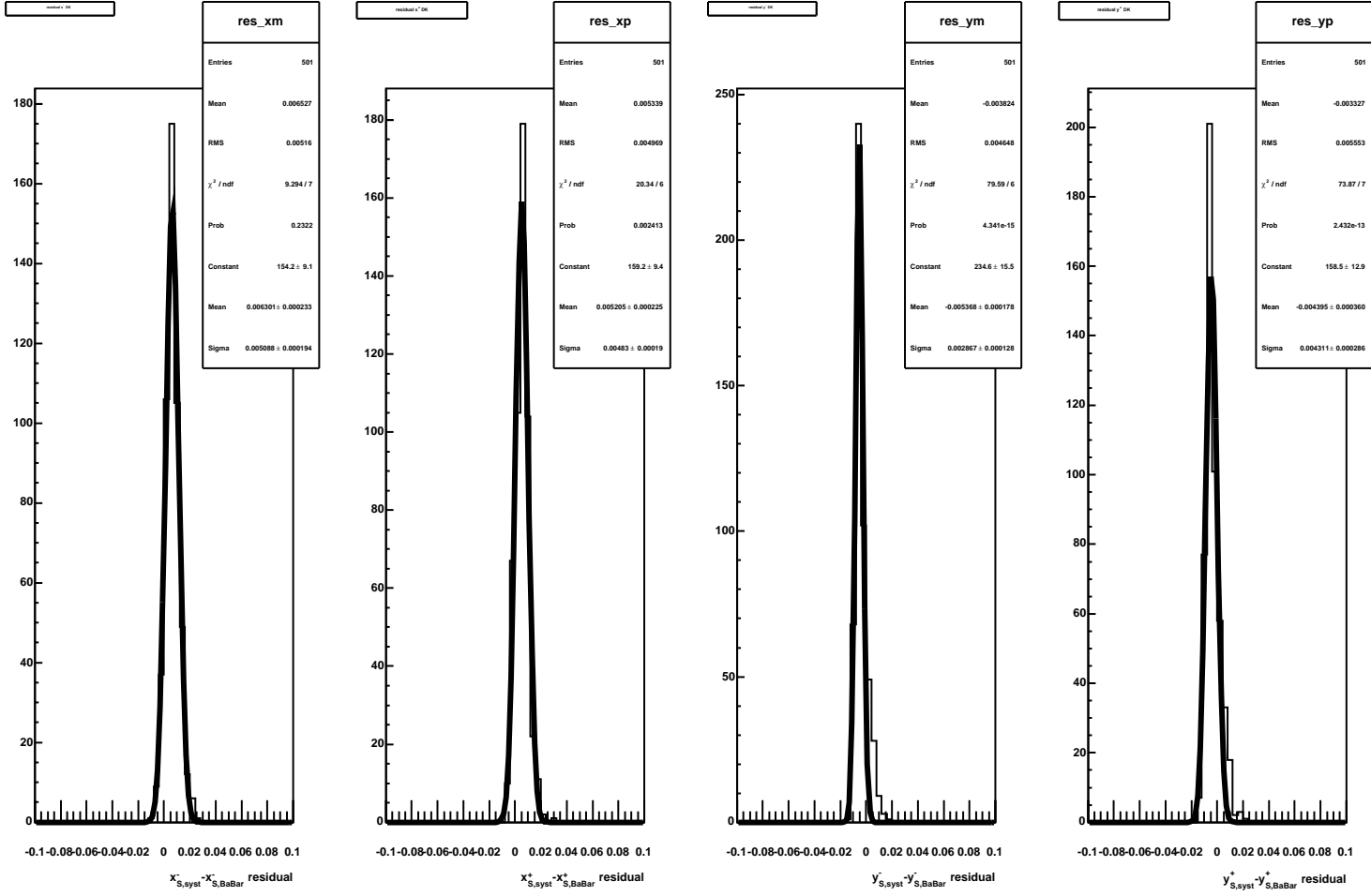


Figure 23: Experiment-by-experiment differences of the cartesian CP fit parameters using the reference and the K-matrix Dalitz models for the  $B^- \rightarrow D^0 K^{*-}$  decay mode. The systematic error for each component is quoted as quadratic sum of the bias and the rms.

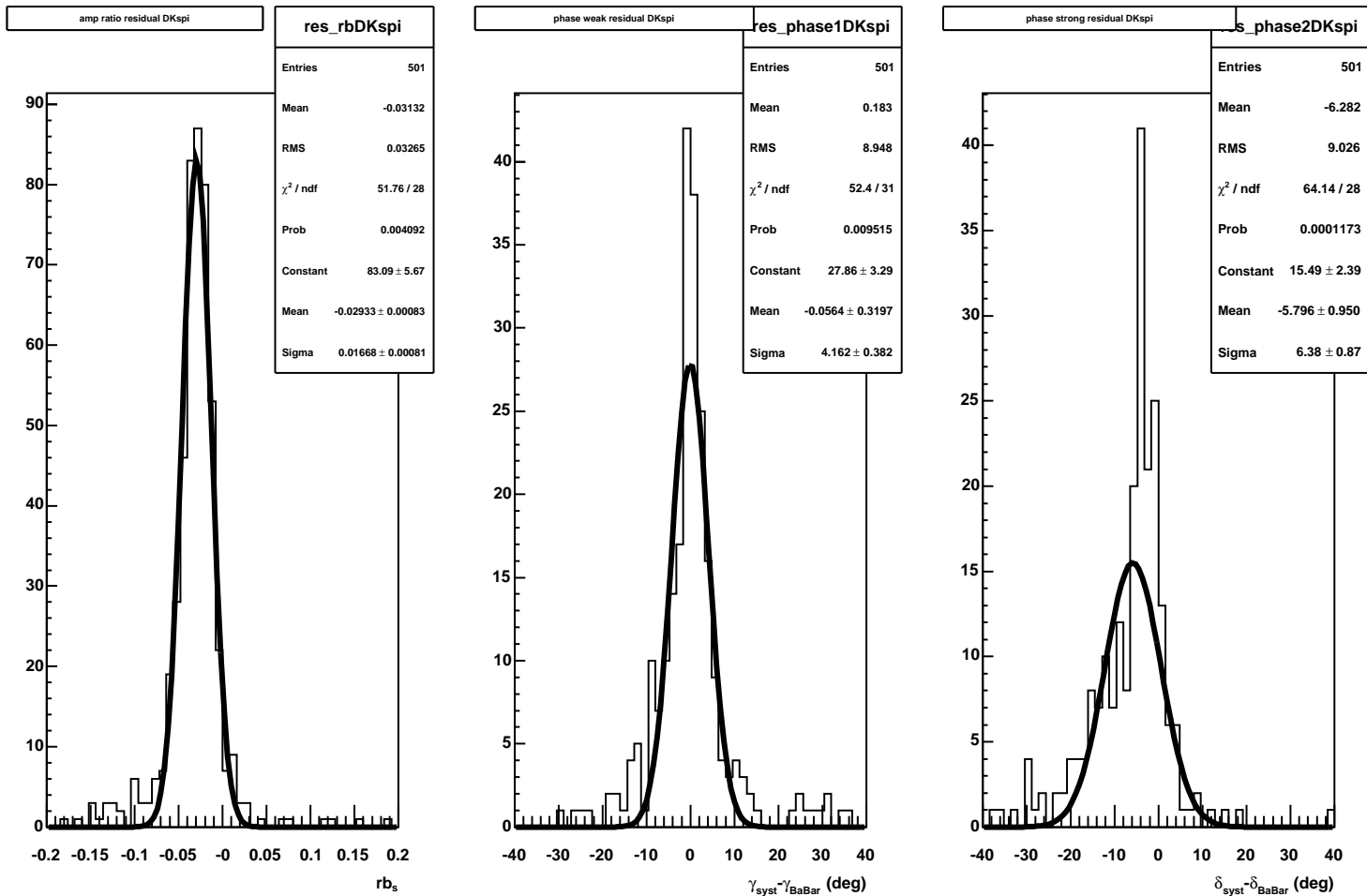


Figure 24: Experiment-by-experiment differences of the  $kr_s$ ,  $\gamma$ ,  $\delta_s$  CP for parameters using the reference and the CLEO Dalitz models for the  $B^- \rightarrow D^0 K^{*-}$  decay mode. The systematic error for each component is quoted as quadratic sum of the bias and the rms.

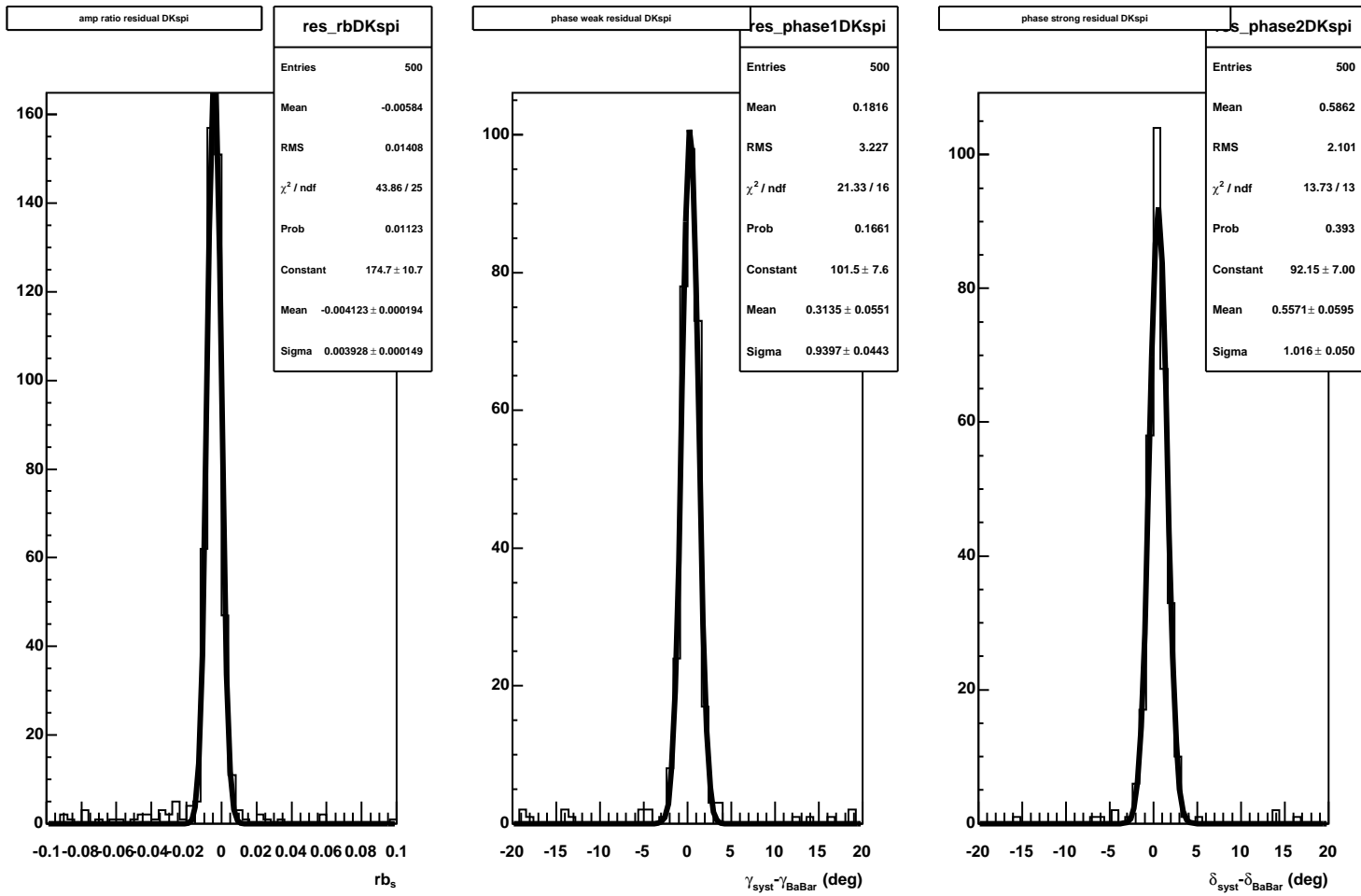


Figure 25: Experiment-by-experiment differences of the  $kr_s$ ,  $\gamma$ ,  $\delta_s$  CP fit parameters using the reference and the K-matrix Dalitz models for the  $B^- \rightarrow D^0 K^{*-}$  decay mode. The systematic error for each component is quoted as quadratic sum of the bias and the rms.

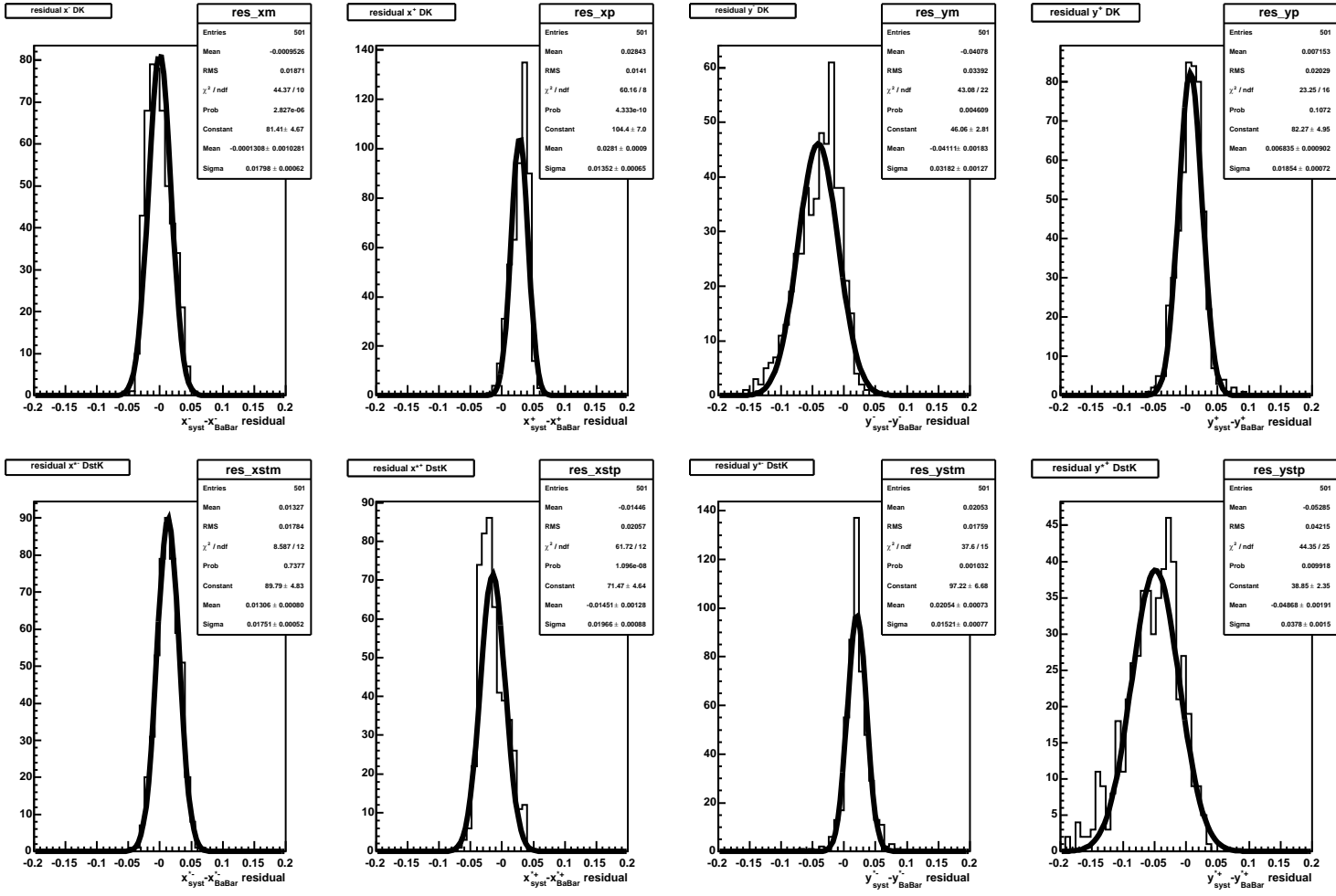


Figure 26: Experiment-by-experiment differences of the cartesian CP fit parameters using the ref-erence and the CLEO Dalitz models for the  $B^- \rightarrow D^{*0} K^-$  decay mode. The systematic error for each component is quoted as quadratic sum of the bias and the rms.

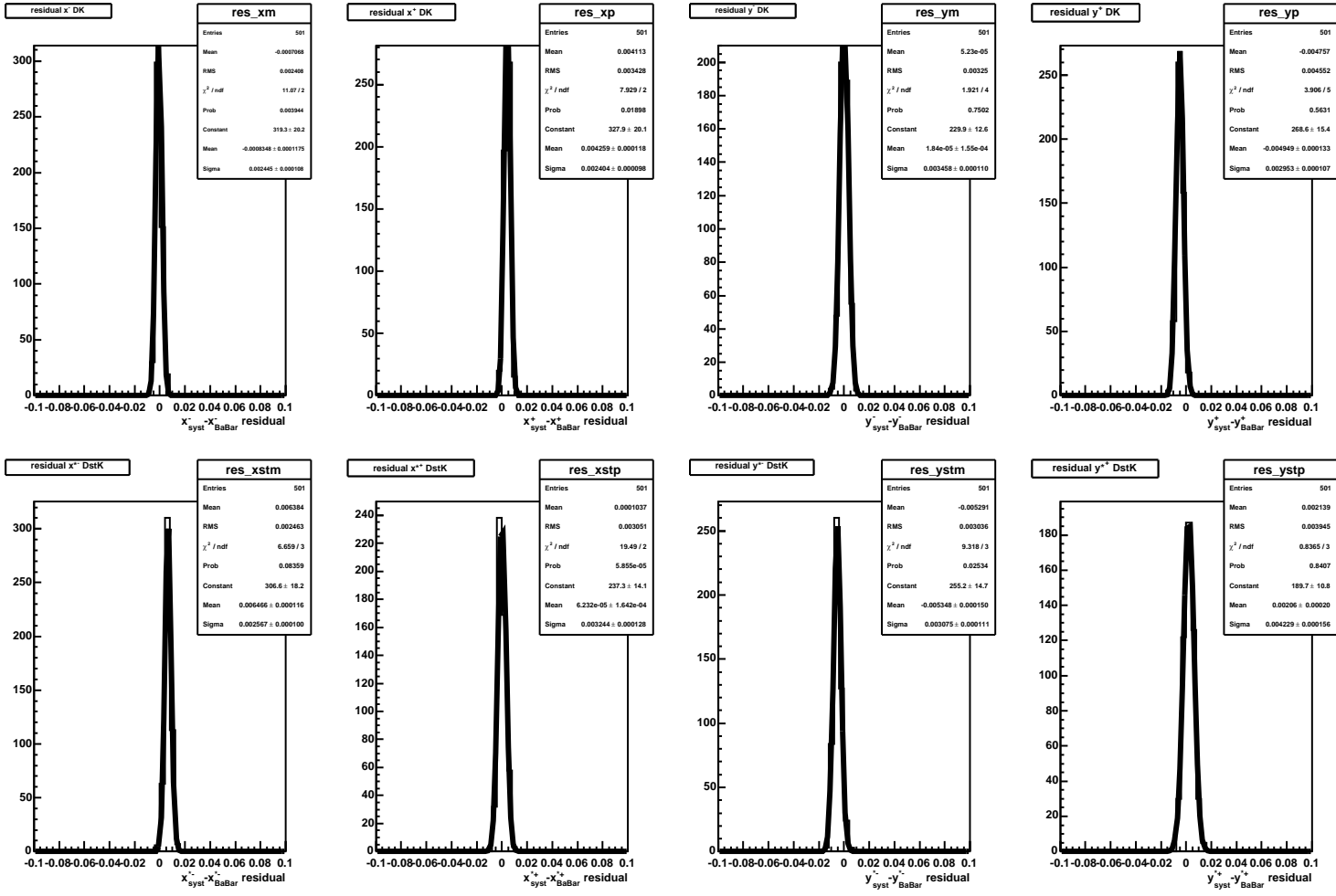


Figure 27: Experiment-by-experiment differences of the cartesian CP fit parameters using the reference and the K-matrix Dalitz models for the  $B^- \rightarrow D^{(*)0} K^-$  decay mode. The systematic error for each component is quoted as quadratic sum of the bias and the rms.

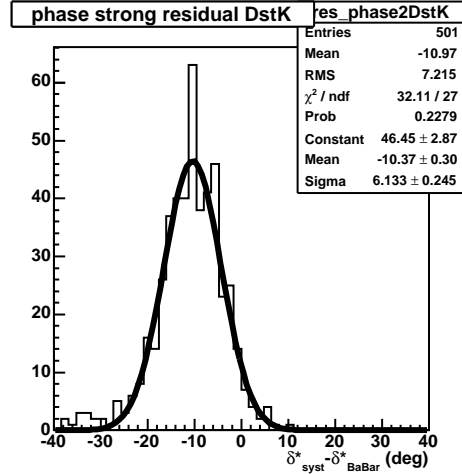
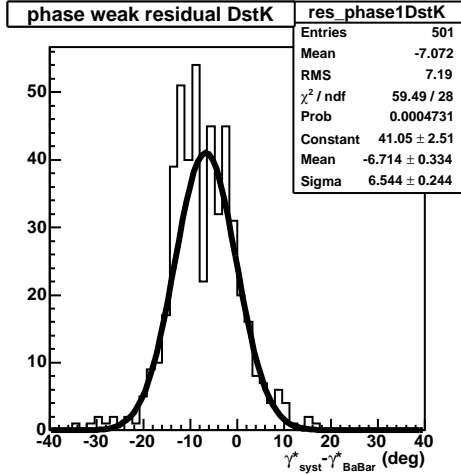
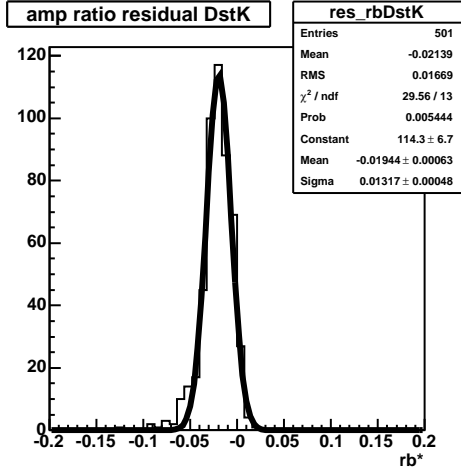
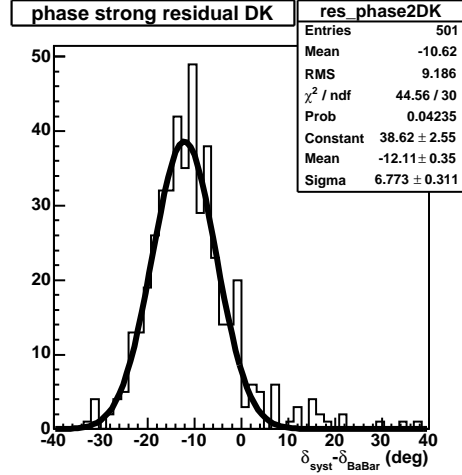
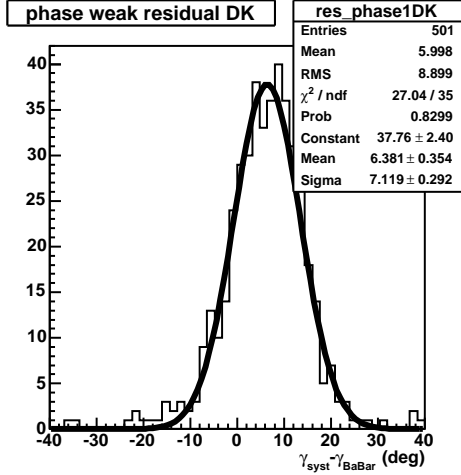
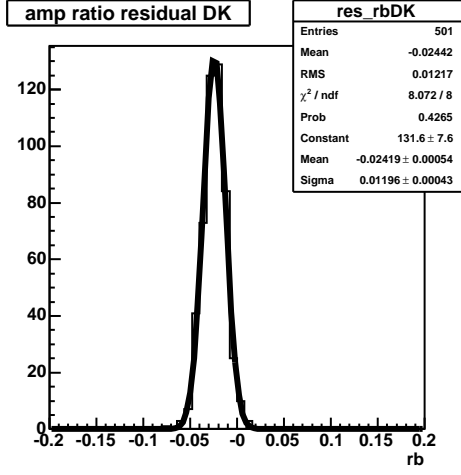


Figure 28: Experiment-by-experiment differences of the  $\tau_B$ ,  $\gamma(D^0K)$ ,  $\delta_B(D^0K)$ ,  $\gamma(D^{*0}K)$ ,  $\delta_B(D^{*0}K)$ ,  $\gamma(D^{*0}K)$ ,  $\delta_B(D^{*0}K)$  CP for parameters using the reference and the CLEO Dalitz models for the  $B^- \rightarrow D^{*0}K^-$  decay mode. The systematic error for each component is quoted as quadratic sum of the bias and the rms.

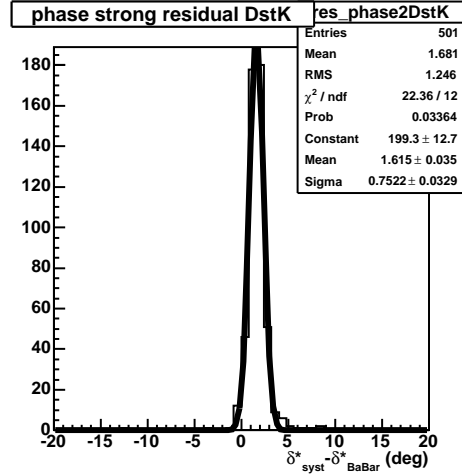
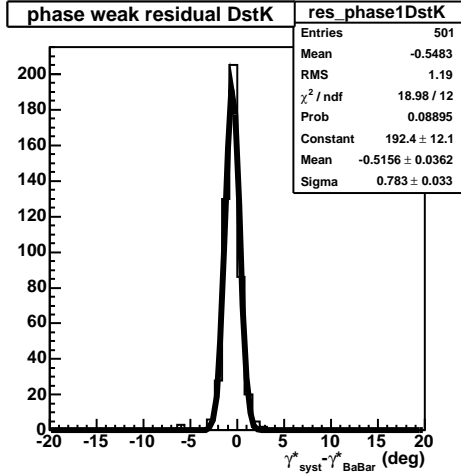
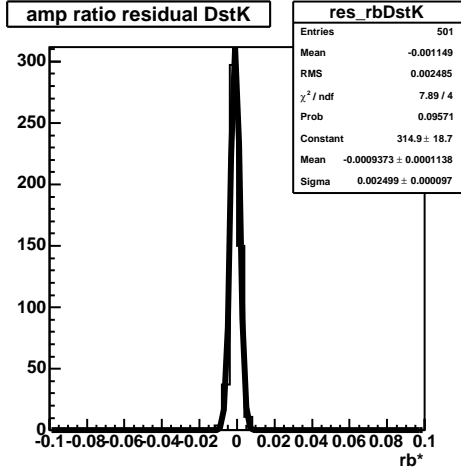
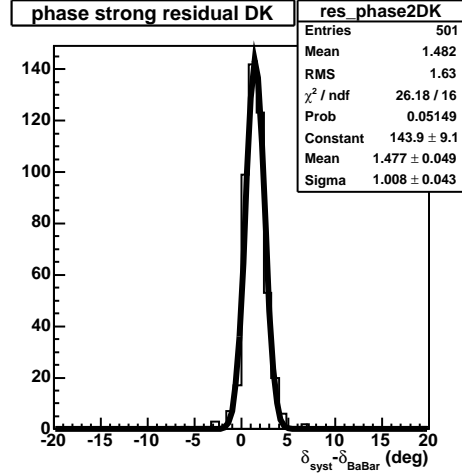
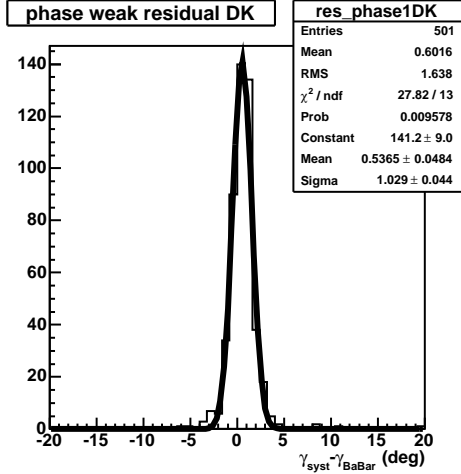
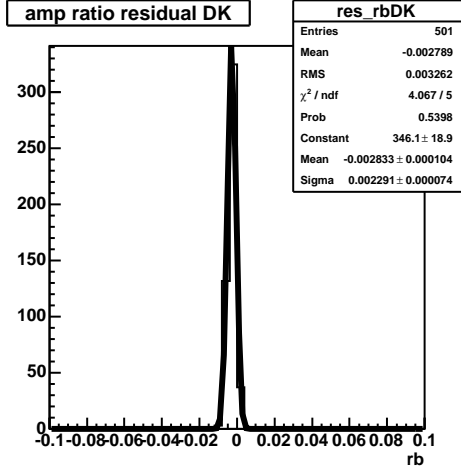


Figure 29: Experiment-by-experiment differences of the  $\tau_B$ ,  $\gamma(D^0K)$ ,  $\delta_B(D^0K)$ ,  $\gamma(D^{*0}K)$ ,  $\delta_B(D^{*0}K)$ ,  $\gamma(D^{*0}K)$  CP fit parameters using the reference and the K-matrix Dalitz models for the  $B^- \rightarrow D^{*0}K^-$  decay mode. The systematic error for each component is quoted as quadratic sum of the bias and the rms.

Source	$r_B$	$\gamma(D^0 K)$ (deg.)	$\delta(D^0 K)$ (deg.)	$r_B^*$	$\gamma(D^{*0} K)$ (deg.)	$\delta_B(D^{*0} K)$ (deg.)
Dalitz model (CLEO)	0.027	10.7	14.0	0.027	10.1	13.1
Dalitz model (K-Matrix)	0.004	1.7	2.2	0.003	1.3	2.1

Table 18: *Systematic errors, due to the  $D^0$  amplitude model, on the physics parameters  $r_B$ ,  $\gamma(D^0 K)$ ,  $\delta_B(D^0 K)$ ,  $r_B^*$ ,  $\gamma(D^{*0} K)$ ,  $\delta_B(D^{*0} K)$  for the  $B^- \rightarrow D^{(*)0} K^-$  decay mode.*

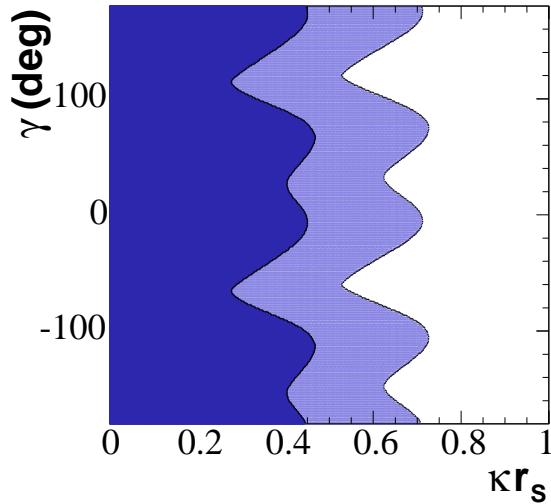


Figure 30: Two-dimensional projections in the  $kr_s - \gamma$  planes of the three-dimensional one- (dark) and two- (light) standard deviation regions, for  $DK^{*\pm}$ .

## 6 Frequentist interpretation of the results

A frequentist analysis [7] has been used to interpret the constraints on  $x_s^\pm$  and  $y_s^\pm$  in terms of  $\mathbf{p} \equiv (kr_s, \delta_s, \gamma)$ . A frequentist (Neyman) construction of the confidence regions of  $\mathbf{p} \equiv (kr_s, \delta_s, \gamma)$  based on the constraints on  $x_s^\pm$  and  $y_s^\pm$  has been adopted [7]. Using a large number of pseudo-experiments corresponding to the nominal  $CP$  fit model but with many different values of the  $CP$  fit parameters, we construct an analytical (Gaussian) parameterization of the PDF of  $(x_s^\pm, y_s^\pm)$  as a function of  $\mathbf{p}$ , as described in [12]. For a given  $\mathbf{p}$ , the three-dimensional confidence level  $\mathcal{C}(\mathbf{p}) = 1 - \alpha(\mathbf{p})$ , where  $\alpha(\mathbf{p})$  is calculated analytically by integrating over all points in the fit parameter space closer (larger PDF) to  $\mathbf{p}$  than the fitted data values. The one (two) standard deviation region of the  $CP$  parameters is defined as the set of  $\mathbf{p}$  values for which  $\alpha(\mathbf{p})$  is smaller than 19.9% (73.8%).

Figures 30 show the two-dimensional projections in the  $kr_s - \gamma$  planes, statistical plus experimental systematic error, for  $DK^{*\pm}$  decay mode. The small statistic of the  $D^0K^*$  signal sample is not sufficient to put significant constraints on the  $\gamma$  value itself. A combined measurement of  $\gamma$  is possible, using the analogous measurement for the  $D^0K$  and  $D^{*0}K$  decay modes. In this case we have a 7-dimensional space for the true parameters  $\mathbf{p} \equiv (r_B, r_B^*, kr_s, \delta_B, \delta_B^*, \delta_s, \gamma)$  and 12 measured cartesian parameters, 4 for each  $D^0K$ ,  $D^{*0}K$ ,  $D^0K^*$  decay mode. Figures 31 show the contours in the  $(x_s^{(*)}, y_s^{(*)})$  planes at 39.3% (dark) and 86.5% (light) probability content and the two-dimensional projections in the  $r_B - \gamma$  and  $kr_s - \gamma$  planes for (d)  $D^0K$ , (e)  $D^{*0}K$ , and (f)  $D^0K^*$ . The errors are statistical plus experimental systematics. The region of 1 (2) sigma equivalent 7D-ellipsoid corresponds to the one where  $\alpha C$  is smaller than 0.52% (22.02%)

The combination yields  $\gamma = (67 \pm 28 \pm 13 \pm 11)^\circ$ , where the first error is statistical, the second is the experimental systematic uncertainty and the third reflects the Dalitz model uncertainty. The contribution to the Dalitz model uncertainty due to the description of the  $\pi\pi$  S-wave in  $D^0 \rightarrow K_s^0 \pi^- \pi^+$  is  $3^\circ$ . From this combination  $kr_s$  is constrained to be  $< 0.50$  ( $0.75$ ) at one (two) standard deviation level. It is worth noting that the value of  $kr_s$  depends on the selected phase

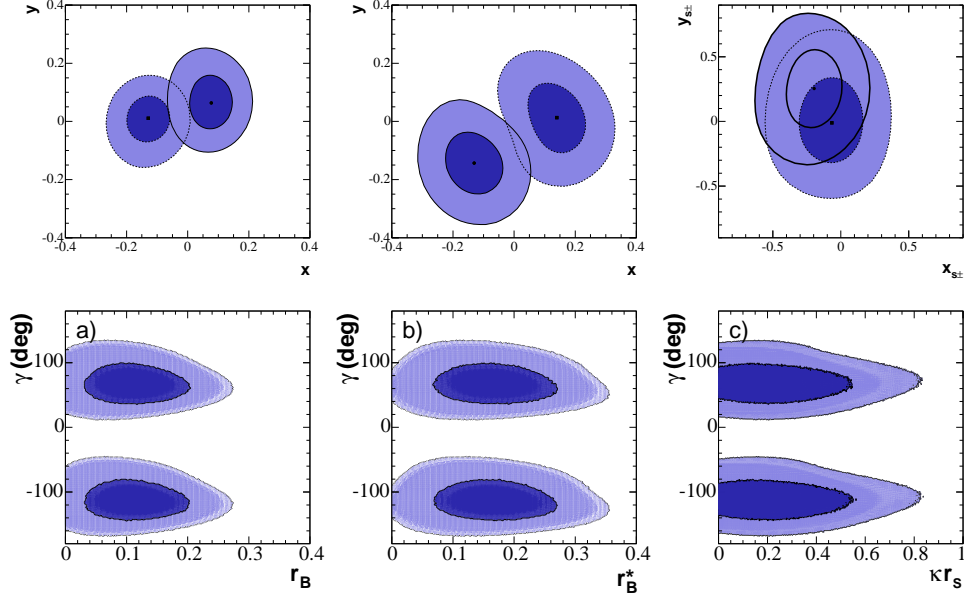


Figure 31: Top row: contours at 39.3% (dark) and 86.5% (light) probability content (statistical only) in the  $(x_{(s)}^{(*)}, y_{(s)}^{(*)})$  planes for (a)  $D^0 K$ , (b)  $D^{*0} K$ , (c)  $D^0 K^*$  separately for  $B^-$  (thick and solid) and  $B^+$  (thin and dotted). Bottom row: two-dimensional projections in the  $r_B - \gamma$  and  $kr_s - \gamma$  planes of the seven-dimensional one- (dark) and two- (light) standard deviation regions, for (d)  $D^0 K$ , (e)  $D^{*0} K$ , and (f)  $D^0 K^*$ .

space region of  $B^- \rightarrow D^0(K_s^0 \pi^-)$  events without introducing any bias on the extraction of  $\gamma$ .

The constraint on  $\gamma$  is consistent with that reported by the Belle Collaboration [14, 15]. However, since our data favor smaller values of  $r_B^{(*)}$  and  $kr_s$  we estimate a larger statistical uncertainty, in agreement with the expected scaling due to the differences in the measured values.

## List of Figures

- 1 *In the top-left plot (green) we show the distribution of the variable for the signal. In the top-right plot the variable distribution for the background. In bottom-left the significance as a function of the cut on the selected variable and in bottom-right the purity (histogram) and the efficiency (point with error bars) as a function of the cut. (Top 4 plots) Sequence of plot described above for the invariant mass of the  $K^{*-}$ . (Bottom 4 plots) Same plots for  $\cos\theta_{Hel}$  of the  $K^{*-}$  daughters. . . . .* 7
- 2 *2D plot of the significance with respect to the cut on the  $K^*$  mass and the cut on  $\cos\theta_{Hel}$ . The color scale represent the value of the significance, it increases from blue to red. The maximum value is 6.2 with  $|m_{K^*} - m_{K^*}(PDG)| < 55 \text{ MeV}/c^2$  and  $|\cos\theta_{Hel}| > 0.35$ . . . . .* 8
- 3 *Unbinned maximum Likelihood fit to the  $m_{ES}$  distribution doesn't show any evidence of  $K_S^0 K_S^0 K^{*-}$  signal events on the  $D^0$  sidebands after all the selection cuts are applied.* 11
- 4 *The fit to the  $D^0$  distribution shows evidence of true  $D^0$  background events. The events are selected in the  $m_{ES}$  sidebands ( $m_{ES} < 5.27 \text{ GeV}/c^2$ ) with all the selection cuts applied. Left: data; Right: Monte Carlo . . . . .* 12
- 5 *Distribution of the number of  $B$  candidates per event after all the cuts applied in the signal region  $m_{ES} > 5.270 \text{ MeV}/c^2$ ,  $|\Delta E| < 25 \text{ MeV}$ . Colored histograms represent background events and point with error bars represent data. . . . .* 13
- 6 *The plots show the data/MC comparison for the relevant variables used in the selection criteria. From the top left to the bottom right the following quantities are reported:  $\cos(\theta_T)$ ,  $D^0$  mass,  $K_S^0$  mass,  $\Delta E$ ,  $K^*$  mass, Fisher,  $\cos\theta_{Hel}$ ,  $m_{ES}$ . The events in the plots are selected applying all the selection criteria but the one on the displayed variable. . . . .* 14
- 7 *Fisher- $m_{ES}$  correlation for  $B^- \rightarrow D^0 K^{*-}$  signal events. Even for background events the correlation was found to be negligible. . . . .* 19
- 8  *$B^- \rightarrow D^0 K^{*-}$   $m_{ES}$  (left column),  $\Delta E$  (middle column) and  $\mathcal{F}$  (right column) shapes from Monte Carlo for Sig (top row), Cont (middle row), and  $B\bar{B}$  (bottom row). The  $\Delta E$  PDF shapes are show only for reference since they are not used in the CP fit. Only the  $B\bar{B}$   $m_{ES}$  shape parameters are fixed to values found in Monte Carlo (as shown in Table 7). The Argus Cont and Gaussian Sig resolution parameters are extracted from the  $B^- \rightarrow D^0 \pi^-$  control sample, while the Gaussian mean value is determined from  $B^- \rightarrow D^0 K^{*-}$  data. The  $\mathcal{F}$  shapes in the final CP fit are extracted from the  $B^- \rightarrow D^0 \pi^-$  control sample (as given in Table 7), while the values indicated in this figure correspond to the Monte Carlo samples. The  $m_{ES}$  distributions are obtained for  $|\Delta E| < 25 \text{ MeV}$ , while the  $\mathcal{F}$  distributions are for  $|\Delta E| < 25$  and  $m_{ES} > 5.272 \text{ GeV}/c^2$ . . . . .* 21
- 9  *$B^- \rightarrow D^0 K^{*-}$  Dalitz efficiency mapping for signal MC (phase space), for  $|\Delta E| < 25 \text{ MeV}$  and  $m_{ES} > 5.2 \text{ GeV}/c^2$  ( $m_{AB}^2 \equiv m_+^2$ ,  $m_{AC}^2 \equiv m_-^2$ ,  $m_{BC}^2 \equiv m_{\pi^+\pi^-}$ ). The blue curve is the result of an unbinned likelihood fit to a second order polynomial (after symmetrization of the Dalitz plot) to the  $B^- \rightarrow D^0 K^{*-}$  signal Monte Carlo, while the red curve corresponds to a phase space distribution. . . . .* 24
- 10  *$B^- \rightarrow D^0 K^{*-}$  Cont background Dalitz shape from generic Monte Carlo, for  $|\Delta E| < 25 \text{ MeV}$  and  $m_{ES} > 5.2 \text{ GeV}/c^2$  ( $m_{AB}^2 \equiv m_+^2$ ,  $m_{AC}^2 \equiv m_-^2$  and  $m_{BC}^2 \equiv m_{\pi^+\pi^-}$ ). The blue curve is the result of an unbinned likelihood fit to a second order polynomial (after symmetrization of the Dalitz plot), while the red curve corresponds to a phase space distribution. . . . .* 25

11	$B^- \rightarrow D^0 K^{*-} \text{B}\bar{\text{B}}$ background Dalitz shape from generic Monte Carlo, for $ \Delta E  < 25$ MeV and $m_{\text{ES}} > 5.2$ GeV/ $c^2$ ( $m_{\text{AB}}^2 \equiv m_+^2$ , $m_{\text{AC}}^2 \equiv m_-^2$ and $m_{\text{BC}}^2 \equiv m_{\pi^+\pi^-}$ ). The blue curve is the result of an unbinned likelihood fit to a second order polynomial (after symmetrization of the Dalitz plot), while the red curve corresponds to a phase space distribution. . . . .	26
12	$B^- \rightarrow D^0 K^{*-} m_{\text{ES}}$ , and $\mathcal{F}$ shapes extracted from the fit in the $\Delta E$ region $[-25, 25]$ MeV, compared to the data. Also shown are the different background components: Sig (red), $\text{B}\bar{\text{B}}$ (green) and Cont (magenta). . . . .	27
13	39.3% (dark blue) and 86.5% (bright blue) confidence-level contours, corresponding to $1\sigma$ and $2\sigma$ two-dimensional ellipsoid regions, in the $(x_{s\pm}, y_{s\pm})$ cartesian fit parameter space for $B^- \rightarrow D^0 K^{*-}$ . Solid (dotted) contours are for $B^-$ ( $B^+$ ) decays. Given the good Gaussian behavior of the cartesian parameters, these contours have been obtained using the standard likelihood ratio method, $\Delta \ln(\mathcal{L}_{\text{exp}}) = 1.0, 4.0$ . . . . .	29
14	$B^- \rightarrow D^0 K^{*-} m_{\text{ES}}$ and $\mathcal{F}$ shapes from the Dalitz CP fit compared to the data. The shapes are fixed to the values found from the shapes prefit while the Sig, Cont and $\text{B}\bar{\text{B}}$ yields are refloated exploiting the Dalitz plot as additional discriminant variable. Also shown are the different background components: Sig (red), $\text{B}\bar{\text{B}}$ (green) and Cont (magenta). . . . .	30
15	$B^- \rightarrow D^0 K^{*-}$ Dalitz plot and their projections from the CP fit for events with $ \Delta E  < 25$ MeV and $m_{\text{ES}} > 5.2$ GeV/ $c^2$ ( $m_{\text{AB}}^2 \equiv m_+^2$ , $m_{\text{AC}}^2 \equiv m_-^2$ , $m_{\text{BC}}^2 \equiv m_{\pi^+\pi^-}$ ). . . . .	31
16	$B^- \rightarrow D^0 K^{*-}$ Dalitz plot and their projections from the CP fit for events with $ \Delta E  < 25$ MeV and $m_{\text{ES}} > 5.272$ GeV/ $c^2$ ( $m_{\text{AB}}^2 \equiv m_+^2$ , $m_{\text{AC}}^2 \equiv m_-^2$ , $m_{\text{BC}}^2 \equiv m_{\pi^+\pi^-}$ ). . . . .	32
17	Residual, error and pull distributions for the $\text{B}\bar{\text{B}}$ (top left in landscape), Cont (top right in landscape) and Sig (bottom in landscape) components for the $B^- \rightarrow D^0 K^{*-}$ sample from the nominal Toy MC. . . . .	33
18	Residual, error and pull distributions for $x_{s+} \equiv \text{re}P$ (top left in landscape), $x_{s-} \equiv \text{re}M$ (top right in landscape), $y_{s+} \equiv \text{im}P$ (bottom left in landscape), and $y_{s-} \equiv \text{im}M$ (top right in landscape), for the $B^- \rightarrow D^0 K^{*-}$ sample for the nominal Toy MC. . . . .	34
19	Residual, error and pull distributions for $r_s^2$ for the $B^- \rightarrow D^0 K^{*-}$ sample for the nominal Toy MC. . . . .	35
20	Distribution of log-likelihood values for the nominal toy MC. The arrow indicates the value obtained in the data set fit. The agreement with expectations is remarkable, providing a goodness-of-fit of about 50%. . . . .	35
21	Residual, error and pull distributions for $x_{s+} \equiv \text{re}P$ (top left in landscape), $x_{s-} \equiv \text{re}M$ (top right in landscape), $y_{s+} \equiv \text{im}P$ (bottom left in landscape), and $y_{s-} \equiv \text{im}M$ (top right in landscape), for the $B^- \rightarrow D^0 K^{*-}$ sample for a Toy MC tuned to the data with $r_s^2$ fixed to 0.04. . . . .	36
22	Experiment-by-experiment differences of the cartesian CP fit parameters using the reference and the CLEO Dalitz models for the $B^- \rightarrow D^0 K^{*-}$ decay mode. The systematic error for each component is quoted as quadratic sum of the bias and the rms. . . . .	41
23	Experiment-by-experiment differences of the cartesian CP fit parameters using the reference and the K-matrix Dalitz models for the $B^- \rightarrow D^0 K^{*-}$ decay mode. The systematic error for each component is quoted as quadratic sum of the bias and the rms. . . . .	42

24	<i>Experiment-by-experiment differences of the <math>kr_s</math>, <math>\gamma</math>, <math>\delta_s</math> CP fit parameters using the reference and the CLEO Dalitz models for the <math>B^- \rightarrow D^0 K^{*-}</math> decay mode. The systematic error for each component is quoted as quadratic sum of the bias and the rms.</i>	43
25	<i>Experiment-by-experiment differences of the <math>kr_s</math>, <math>\gamma</math>, <math>\delta_s</math> CP fit parameters using the reference and the K-matrix Dalitz models for the <math>B^- \rightarrow D^0 K^{*-}</math> decay mode. The systematic error for each component is quoted as quadratic sum of the bias and the rms.</i>	44
26	<i>Experiment-by-experiment differences of the cartesian CP fit parameters using the reference and the CLEO Dalitz models for the <math>B^- \rightarrow D^{(*)0} K^-</math> decay mode. The systematic error for each component is quoted as quadratic sum of the bias and the rms.</i>	45
27	<i>Experiment-by-experiment differences of the cartesian CP fit parameters using the reference and the K-matrix Dalitz models for the <math>B^- \rightarrow D^{(*)0} K^-</math> decay mode. The systematic error for each component is quoted as quadratic sum of the bias and the rms.</i>	46
28	<i>Experiment-by-experiment differences of the <math>r_B</math>, <math>\gamma(D^0 K)</math>, <math>\delta_B(D^0 K)</math>, <math>\gamma(D^{*0} K)</math>, <math>\delta_B(D^{*0} K)</math> CP fit parameters using the reference and the CLEO Dalitz models for the <math>B^- \rightarrow D^{(*)0} K^-</math> decay mode. The systematic error for each component is quoted as quadratic sum of the bias and the rms.</i>	47
29	<i>Experiment-by-experiment differences of the <math>r_B</math>, <math>\gamma(D^0 K)</math>, <math>\delta_B(D^0 K)</math>, <math>\gamma(D^{*0} K)</math>, <math>\delta_B(D^{*0} K)</math> CP fit parameters using the reference and the K-matrix Dalitz models for the <math>B^- \rightarrow D^{(*)0} K^-</math> decay mode. The systematic error for each component is quoted as quadratic sum of the bias and the rms.</i>	48
30	<i>Two-dimensional projections in the <math>kr_s - \gamma</math> planes of the three-dimensional one- (dark) and two- (light) standard deviation regions, for <math>DK^{*\pm}</math>.</i>	50
31	<i>Top row: contours at 39.3% (dark) and 86.5% (light) probability content (statistical only) in the <math>(x_{(s)}^{(*)}, y_{(s)}^{(*)})</math> planes for (a) <math>D^0 K</math>, (b) <math>D^{*0} K</math>, (c) <math>D^0 K^*</math> separately for <math>B^-</math> (thick and solid) and <math>B^+</math> (thin and dotted). Bottom row: two-dimensional projections in the <math>r_B - \gamma</math> and <math>kr_s - \gamma</math> planes of the seven-dimensional one- (dark) and two- (light) standard deviation regions, for (d) <math>D^0 K</math>, (e) <math>D^{*0} K</math>, and (f) <math>D^0 K^*</math>.</i>	51

## List of Tables

1	<i>Number of generated Monte Carlo events for signals and backgrounds and corresponding integrated luminosities. The integrated luminosity for data is also given. . .</i>	5
2	<i>Branching fractions and cross sections used to get the values of Table 1. These values have been used to normalize the signal and the different background components. . .</i>	6
3	<i>Results from the gaussian fit of the <math>\Delta E</math> distribution on signal Monte Carlo sample. .</i>	6
4	<i>Results from the gaussian fit of the <math>K_S^0</math> mass distribution on data and Monte Carlo samples. . . . .</i>	9
5	<i>Efficiency (ratio of fully matched combinations over total number of signal events) and background rejection rates (number of combinations over total number of background events for each sample) after each cut, with <math>m_{ES} &gt; 5.2</math>. Binomial errors are reported. Purity and significance in the signal box region (<math>m_{ES} &gt; 5.270 \text{ GeV}/c^2</math> and <math> \Delta E  &lt; 0.025 \text{ GeV}</math>). . . . .</i>	10
6	<i><math>D^0</math> fractions for background events are estimated from generic MC and data, for the region <math> \Delta E  &lt; 25 \text{ MeV}</math> and <math>m_{ES} &gt; 5.2 \text{ GeV}/c^2</math>. In data we have restricted the <math>m_{ES}</math> region to <math>5.2 &lt; m_{ES} &lt; 5.27 \text{ GeV}/c^2</math> to exclude the signal events. . . . .</i>	11
7	<i><math>B^- \rightarrow D^0 K^{*-}</math> shape parameters as extracted from the <math>m_{ES}</math> and <math>\mathcal{F} B^- \rightarrow D^0 K^{*-}/B^- \rightarrow D^0 \pi^-</math> combined fit. Only the <math>B\bar{B}</math> <math>m_{ES}</math> shapes are taken from simulation. . . . .</i>	22
8	<i>The values and the errors for the parameters of the third-order polynomial function, Eq. (19), obtained from the unbinned likelihood fit to the efficiency and Dalitz shape backgrounds for <math>B^- \rightarrow D^0 K^{*-}</math> events after symmetrization of the Dalitz plot (<math>m_+^2</math> vs <math>m_-^2</math>), for <math> \Delta E  &lt; 25 \text{ MeV}</math> and <math>m_{ES} &gt; 5.2 \text{ GeV}/c^2</math>. . . . .</i>	23
9	<i><math>B^- \rightarrow D^0 K^{*-}</math> <math>D^0</math> fractions as estimated from generic MC, for the region <math> \Delta E  &lt; 25 \text{ MeV}</math> and <math>m_{ES} &gt; 5.2 \text{ GeV}/c^2</math>. . . . .</i>	23
10	<i><math>B^- \rightarrow D^0 K^{*-}</math> yields from PDF shapes fit in <math>\Delta E \in [-25, 25] \text{ MeV}</math> region. . . . .</i>	24
11	<i>Fit results on data for <math>(x_{s\pm}, y_{s\pm})</math> cartesian coordinates for the <math>B^- \rightarrow D^0 K^{*-}</math> decay mode. The values inside brackets are the quadratic (Gaussian) errors calculated from the fit covariance matrix. . . . .</i>	28
12	<i>Correlation matrix for <math>(x_{s\pm}, y_{s\pm})</math> cartesian coordinates, for the <math>B^- \rightarrow D^0 K^{*-}</math> decay mode. . . . .</i>	28
13	<i><math>B^- \rightarrow D^0 K^{*-}</math> yields from the CP fit. . . . .</i>	28
14	<i>Summary of the contributions to the systematic error in cartesian coordinates <math>(x_{s\pm}, y_{s\pm})</math>. 37</i>	
15	<i>Systematic errors, due to the <math>D^0</math> amplitude model, on the cartesian coordinates, <math>(x_{s\pm}, y_{s\pm})</math> for the <math>B^- \rightarrow D^0 K^{*-}</math> decay mode. . . . .</i>	40
16	<i>Systematic errors, due to the <math>D^0</math> amplitude model, on the physics parameters, <math>kr_s</math>, <math>\gamma</math>, <math>\delta_s</math> for the <math>B^- \rightarrow D^0 K^{*-}</math> decay mode. . . . .</i>	40
17	<i>Systematic errors, due to the <math>D^0</math> amplitude model, on the cartesian coordinates <math>(x_{\pm}, y_{\pm}, x_{\pm}^*, y_{\pm}^*)</math> for the <math>B^- \rightarrow D^{(*)0} K^-</math> decay mode. . . . .</i>	40
18	<i>Systematic errors, due to the <math>D^0</math> amplitude model, on the physics parameters <math>r_B</math>, <math>\gamma(D^0 K)</math>, <math>\delta_B(D^0 K)</math>, <math>r_B^*</math>, <math>\gamma(D^{*0} K)</math>, <math>\delta_B(D^{*0} K)</math> for the <math>B^- \rightarrow D^{(*)0} K^-</math> decay mode. .</i>	49

## A Model dependent parametrization of the $B^- \rightarrow D^0 K^{*-}$ amplitude

We have written the decay amplitude and rate in the most general way in Eqs. (5) and (6). To give a complete picture, in the following part of the section, till eq. 27, we'll describe how the quantities  $r_s^2$ ,  $x_{s\pm}$  and  $y_{s\pm}$  in eq. 15 are related to the analogous quantities for the  $B^- \rightarrow DK^{*-}$  and  $B^- \rightarrow D(K\pi)_{\text{non-}K^*}^-$  parts. However, we want to stress that the measurement of  $\gamma$  is done by extracting  $r_s^2$ ,  $x_{s\pm}$  and  $y_{s\pm}$  with the PDF in eq. 15 and we don't need to know anything else.

We split explicitly the amplitude in a resonant ( $B^- \rightarrow DK^{*-}$ ) and non-resonant ( $B^- \rightarrow D(K\pi)_{\text{non-}K^*}^-$ ) part, and we make explicit the dependence on the  $(K\pi)^-$  helicity angle  $\theta_H$  taking into account that the signal component is p-wave and the non- $K^*$  is s-wave (this is an assumption). The result obtained in eq. 22 is still valid for a P- or D- wave assumption, if the neglect possible distortions from a non-omogenous reconstruction efficiency). We write Eqs. (5) and (6) as:

$$A(B^- \rightarrow (D[\rightarrow f]X_s^-)_p) = \sqrt{\frac{3}{2}} \cos \theta_H A_{fp}^{K^*} + \sqrt{\frac{1}{2}} A_{fp}^{\text{non-}K^*}, \quad (20)$$

$$\Gamma(B^- \rightarrow (D[\rightarrow f]X_s^-)) = \frac{3}{2} \cos^2 \theta_H \int dp |A_{fp}^{K^*}|^2 + \frac{1}{2} \int dp |A_{fp}^{\text{non-}K^*}|^2 + \sqrt{3} \cos \theta_H \int dp \text{Re}[A_{fp}^{K^*} (A_{fp}^{\text{non-}K^*})^*] \quad (21)$$

where  $A_{fp}^{K^*}$  is the contribution of  $B \rightarrow DK^*$  and  $A_{fp}^{\text{non-}K^*}$  is the contribution of  $B^- \rightarrow D(K\pi)_{\text{non-}K^*}$ . If we consider the decay rate after integrating over the helicity angle, the interference term cancels out:

$$\Gamma(B^- \rightarrow (D[\rightarrow f]X_s^-)) = \int dp |A_{fp}^{K^*}|^2 + \int dp |A_{fp}^{\text{non-}K^*}|^2. \quad (22)$$

The cancellation of the interference term proportional to  $\cos \theta_H$  simplifies the relationships a lot and reduces significantly the effect of the non-resonant contribution, but it's not strictly valid if the experimental efficiency is not symmetric over  $\cos \theta_H$ . Therefore the validity of this assumption will be checked and if necessary a systematic error will be assigned. Integrating over the helicity angle  $\theta_H$  and using the result in Eq. (22), Eq. (15) transforms to

$$\Gamma(B^\mp \rightarrow D[\rightarrow K_S^0 \pi^- \pi^+] K^{*\mp}) \propto |f_\mp|^2 + \frac{(r_{sR}^2 + \rho_c^2 r_{sNR}^2)}{1 + \rho_c^2} |f_\pm|^2 + 2 \left[ \frac{(x_{sR\mp} + \rho_c^2 x_{sNR\mp})}{1 + \rho_c^2} \text{Re}[f_\mp f_\pm^*] + \frac{(y_{sR\mp} + \rho_c^2 y_{sNR\mp})}{1 + \rho_c^2} \text{Im}[f_\mp f_\pm^*] \right], \quad (23)$$

where

$$\begin{aligned} x_{sR\pm} &= \text{Re}[k_R r_{sR} e^{i(\delta_{sR} \pm \gamma)}], \\ y_{sR\pm} &= \text{Im}[k_R r_{sR} e^{i(\delta_{sR} \pm \gamma)}], \\ x_{sNR\pm} &= \text{Re}[k_{NR} r_{sNR} e^{i(\delta_{sNR} \pm \gamma)}], \\ y_{sNR\pm} &= \text{Im}[k_{NR} r_{sNR} e^{i(\delta_{sNR} \pm \gamma)}], \end{aligned} \quad (24)$$

with  $\rho_c^2 \equiv \left| \frac{A(B^- \rightarrow D^0 (K\pi)_{\text{non-}K^*}^-)}{A(B^- \rightarrow D^0 K^{*-})} \right|_{\text{cut}}^2$  the fraction of the non-resonant contribution with respect to the  $B^- \rightarrow D^0 K^{*-}$  signal. An estimate of this quantity,  $\rho_c^2 \sim 0.048$ , has been performed by for the GLW and ADS analysis and it's documented in ref. [8, 9]. The value of  $\rho_c^2$  generally depends

on the selection requirements, however those analysis applied almost identical cuts therefore the estimate can be considered attendable also for our selection. Here, the “k-factors” accounts for any possible dependence of  $r_B$  and  $\delta_B$  over the  $(K\pi)^-$  mass system (either resonant or non-resonant). Comparing each term of Eq. (23) and (15) we find:

$$r_s^2 \rightarrow \frac{r_{sR}^2 + \rho_c^2 r_{sNR}^2}{1 + \rho_c^2}, \quad (25)$$

$$x_{s\mp} \rightarrow \frac{x_{sR\mp} + \rho_c^2 x_{sNR\mp}}{1 + \rho_c^2}, \quad (26)$$

$$y_{s\mp} \rightarrow \frac{y_{sR\mp} + \rho_c^2 y_{sNR\mp}}{1 + \rho_c^2}. \quad (27)$$

This model dependent parameterization in principle would allow to evaluate the relative amount of resonant and non-resonant contribution in the  $B^\pm \rightarrow D(K_S^0\pi^\pm)$  decay. Since it has been demonstrated with ToyMC experiments that it is possible to extract the  $r_s^2$  parameter from data, this parameterization is not useful for the analysis, however we decided to leave it in the appendix as reference.

## B Considerations on the efficiency variation over the $B^- \rightarrow D^0 K_S^0 \pi^-$ Dalitz plot

The general parametrization of the PDFs in terms of  $\{r_s^2, x_{s\pm}, y_{s\pm}\}$  in eq. 15 of section 2 applies to the general case where the reconstruction efficiency of the  $B$  decay varies over the  $B \rightarrow DK_S^0 \pi$  phase space. Let us consider eq. 6 and suppose that the relation holds when the reconstruction efficiency is uniform over the  $B$  phase space. In the general case where the efficiency is not uniform we need to introduce a factor  $\epsilon(p)$  multiplying each term of the right-hand side of 6, where  $p$  is the point in the  $B$  phase space. Eq. 6 can be written as:

$$\Gamma(B^- \rightarrow D[\rightarrow f]X_s^-) = \int dp \left( A_{cp}^2 A_f^2 + A_{up}^2 A_{\bar{f}}^2 + 2A_{cp} A_f A_{up} A_{\bar{f}} \text{Re}(e^{i(\delta_p + \delta_D - \gamma)}) \right) \epsilon(p). \quad (28)$$

If we define  $A'_{cp} \equiv A_{cp} \sqrt{\epsilon(p)}$  and  $A'_{up} \equiv A_{up} \sqrt{\epsilon(p)}$  eq. 28 becomes:

$$\Gamma(B^- \rightarrow D[\rightarrow f]X_s^-) = \int dp \left( A'^2_{cp} A_f^2 + A'^2_{up} A_{\bar{f}}^2 + 2A'_{cp} A_f A'_{up} A_{\bar{f}} \text{Re}(e^{i(\delta_p + \delta_D - \gamma)}) \right). \quad (29)$$

Defining  $r_s$ ,  $k$  and  $\delta_s$  as:

$$r_s^2 = \frac{\int dp A'^2_{up}}{\int dp A'^2_{cp}}, \quad (30)$$

$$k e^{i\delta_s} = \frac{\int dp A'_{cp} A'_{up} e^{i\delta_p}}{\sqrt{\int dp A'^2_{cp} \int dp A'^2_{up}}}, \quad (31)$$

we obtain again the eq. 15

$$\Gamma(B^\mp \rightarrow D[\rightarrow K_S^0 \pi^- \pi^+]X_s^\mp) \propto |f_\mp|^2 + r_s^2 |f_\pm|^2 + 2 [x_{s\mp} \text{Re}[f_\mp f_\pm^*] + y_{s\mp} \text{Im}[f_\mp f_\pm^*]], \quad (32)$$

where again  $x_{s\pm} = \text{Re}[k r_s e^{i(\delta_s \pm \gamma)}]$  and  $y_{s\pm} = \text{Im}[k r_s e^{i(\delta_s \pm \gamma)}]$ .

Therefore a non-uniform reconstruction efficiency over the  $B$  phase space affects the value of  $r_s$ ,  $k$  and  $\delta_s$ , but the functional form of the PDF (eq. 32) does not change.

## References

- [1] N. Cabibbo, *Phys. Rev. Lett.* **10**, 531 (1963);  
M. Kobayashi and T. Maskawa, *Prog. Theor. Phys.* **49**, 652 (1973).
- [2] B. Aubert *et al.* [BABAR Collaboration], arXiv:hep-ex/0408088.
- [3] B. Aubert *et al.* [BABAR Collaboration], arXiv:hep-ex/0504039.
- [4] *BABAR* Analysis Document, BAD#899.
- [5] *BABAR* Analysis Document, BAD#1237.
- [6] <http://www.slac.stanford.edu/BFROOT/www/Physics/Analysis/AWG/EHBDOC/skims/BchToD0KKstarAll.html>
- [7] PDG 2004.
- [8] J. Chauveau, M. John, R. Kass, G. Therin, BAD#697.
- [9] J. Chauveau, M. John, R. Kass, G. Therin, BAD#1141.
- [10] M. Gronau, *Phys. Lett.* **B557**, 198-206 (2003).
- [11] Belle Collaboration, hep-ex/0504013.
- [12] *BABAR* Analysis Document, BAD#1086.
- [13] A. Palano, Dalitz plot analysis of  $D^0 \rightarrow K_S^0 \pi^+ \pi^-$ ,  $D^0 \rightarrow K_S^0 K^+ \pi^-$ , and  $D^0 \rightarrow K_S^0 K^+ K^-$ ,  
BAD#120.
- [14] The Belle Collaboration, A. Poluektov *et al.*, *Phys. Rev. D* **70**, 072003 (2004); K. Abe *et al.*,  
hep-ex/0411049.
- [15] The Belle Collaboration, K. Abe *et al.*, hep-ex/0504013.